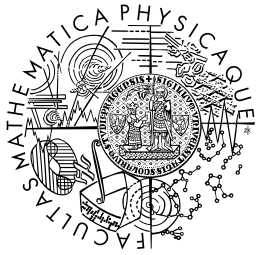

FACULTY
OF MATHEMATICS
AND PHYSICS
Charles University

BACHELOR THESIS

Daniel Dupkala

High resolution spectroscopy of exoplanets - tool for characterization

Department of Atmospheric Physics

Supervisor of the bachelor thesis: Dr. Petr Kabáth
Study programme: Physics
Study branch: Applied physics

Prague 2019

I declare that I carried out this bachelor thesis independently, and only with the cited sources, literature and other professional sources.

I understand that my work relates to the rights and obligations under the Act No. 121/2000 Sb., the Copyright Act, as amended, in particular the fact that the Charles University has the right to conclude a license agreement on the use of this work as a school work pursuant to Section 60 subsection 1 of the Copyright Act.

In Prague on May 16th, 2019 signature of the author

I would like to thank to my supervisor Dr. Petr Kabath for the opportunity to work at the Ondrejov observatory and for all his help and guidance which led me through months of work at the institute and resulted in finishing this bachelor thesis.

I would also like to thank to Dr. Marek Skarka who's work on the optimization of IRAF data reduction pipeline for the OES spectrograph was crucial for the accurate results of my work. My thank belongs to my other colleagues as well for their help and consulting in various stages of my work. Without a great work done by exoplanet group collecting of such amount of data would not be possible. I appreciate the help from Dr. David Jones with modelling of the RM effect and Dr. Miroslav Šlechta's notes about the OES construction. Many thanks belong to the telescope operators as well.

Last but not least, I would like to thank to my family and my parents in particular for their endless support. It was truly encouraging. I want to thank to my friends for their help and support as well. They pushed me when the finish was close but still far away.

Title: High resolution spectroscopy of exoplanets - tool for characterization

Author: Daniel Dupkala

Department: Department of Atmospheric Physics

Supervisor: Dr. Petr Kabáth, Astronomical Institute of the Czech Academy of Sciences

Abstract:
We observed 211 spectra of transiting exoplanet MASCARA-2b (also known as KELT-20b) with OES echelle spectrograph installed at Perek telescope at Astronomical Institute of Czech Academy of Sciences. All data were acquired in 2018. From the total number of observed frames 100 were acquired during transit phase. Spectroscopic time series taken during transit can reveal characteristics of the exoplanet itself. In this work we will present data reduction of the echelle spectroscopy along with analysis of the reduced data. We discuss suitability of the data from Perek telescope for further characterization of exoplanetary systems. We will present the detection limits in this work. Expected aim is to understand the systematic errors and the data sets from Perek telescope in general and their suitability for spectroscopic follow-up in the era of bright TESS exoplanet host stars.

Keywords: Exoplanets, Methods: Spectroscopic, Methods: radial velocities

Contents

Introduction **2**

1 Exoplanet research **4**
1.1 Detection methods 6
1.1.1 Transit photometry 6
1.1.2 Radial velocity measurements 7

2 The instrumentation **10**
2.1 Perek telescope 10
2.2 Ondřejov Echelle Spectrograph 11

3 Observational data set **13**
3.1 Target selection 14
3.2 Data set 14
3.3 Correction frames 15

4 Data reduction **19**
4.1 Image reduction 19
4.2 Spectra identification 21
4.3 Radial velocity determination 22
4.3.1 Telluric lines correction 22
4.3.2 Telluric lines shift 22
4.3.3 Heliocentric correction 22
4.3.4 Template for cross-correlation 23

5 Results **25**
5.1 Basic radial velocity measurements 25
5.2 Transit observations 26
5.3 Rossiter-McLaughlin effect 26
5.4 Limits of OES 27

Summary **32**

References **33**

List of Figures **37**

List of Tables **39**

List of Abbreviations **40**

A Attachments **41**
A.1 Results of RV measurements 41

Introduction

A mankind has always been interested in the existence of life in the universe. However, until the last century the discussion took place only on a theoretical level. Naturally, people have realized that it is necessary to look for extrasolar planets orbiting remote stars.

The first modern attempt to scientifically research existence of exoplanets came with a proposal from Otto Struve in 1952 (Struve 1952 [49]). He calculated the feasibility of the radial velocity method for Jupiter sized planets. A huge progress was made in the 1980s as Bruce Campbell and Gordon Walker developed very precise method for radial velocity measurements (Campbell & Walker 1979 [9]). They reached an accuracy of $15\,\mathrm{m\cdot s^{-1}}$.

Although search for the exoplanets was aimed at the main sequence stars, the first exoplanets were discovered orbiting a pulsar star (Wolszczan & Frail 1992 [56], Wolszczan 1994 [56]). Only in 1995 the first planet orbiting a Sun-like star was reported by Mayor and Queloz (Mayor & Queloz 1995 [28]). The exoplanet was different than any known planet of the Solar system. It was a Jupiter-like gas giant orbiting the 51 Pegasi star on a very close orbit with semi-major axis only 0.0527 AU (Marcy et al. 1997 [26]). This discovery obtained by measuring of very precise radial velocities of the host stars opened door for detection and a characterization of exoplanets.

Since 2000s space telescopes have been used for systematic search for exoplanets. The first was CoRoT mission (Baglin et al. 2006 [3]). It was specially designed for the photometric detection of exoplanets and characterization of stellar pulsations. After CoRoT, the Kepler/K2 mission was launched (Borucky 2016 [6]). Using the transit photometry, Kepler space telescope discovered more than 5000 exoplanet candidates. More than 3000 of the candidates have been already confirmed as the exoplanets.

However, in order to obtain the radius and the mass of the planet both spectroscopic and photometric data need to be combined. Therefore, a spectroscopic ground base follow-up observations are absolutely necessary (Santerne et al. 2013 [43]). As the Jupiter sized candidates and brown dwarf candidates usually present radial velocity semi-amplitude about a few hundreds of $\mathrm{m\cdot s^{-1}}$ they are ideal targets for 2-m class telescopes equipped with state of the art spectrographs capable of measurements of radial velocity variations down to a few tens of $\mathrm{m\cdot s^{-1}}$ (Kabáth et al. 2019 [22]).

For the follow-up observations of the exoplanet candidates a 2-meter Perek telescope at the Astronomical Institute of the Czech Academy of Sciences can be used (Kabáth et al. 2019 [21]). The main instrument used for exoplanet detection and characterization at Perek telescope is the OES — Ondřejov Echelle Spectrograph (Koubský et al. 2004 [23]).

In this thesis we explore suitability of the data from OES for the follow-up observations of the candidates discovered by the space mission TESS. The mission targets bright stars. Therefore, we expect it will be possible to use the data from our follow-up observations for determining whether the candidate is an exoplanet or it is just a false positive (Kabáth et al. 2019 [22]). If precise enough, we expect further characterization of the planetary system will be possible (e.g. detection of

the Rossiter-McLaughlin effect; Narita et al. 2010 [32]). For the spectra analysis we chose an A-type star MASCARA-2 with confirmed giant exoplanet.

In the first chapter basic methodology of the exoplanet research is described. We focus especially on the method of radial velocity measurements. In the second chapter the instrumentation is described in detail. In the third chapter there is a description of the chosen star and the whole data set. In the fourth and the fifth chapter we discuss the data reduction and our results for MASCARA-2b processed according to this pipeline.

1. Exoplanet research

In January 1992 Aleksander Wolszczan and Dale Frail announced the discovery of a very first extrasolar planet (Wolszczan & Frail 1992 [56]). They studied a timing variations of the pulsar PSR 1257+12, from which they concluded two planet-like objects are the cause of these irregular pulses. As the existence of two exoplanets was confirmed later by other studies, they are considered to be the first exoplanets discovered. In 1994 even the third planet was discovered in the system (Wolszczan 1994 [55]). This discovery of the exoplanets orbiting a pulsar was surprising since the pulsar is basically a dead star – a neutron star with the fast rotation and a strong magnetic field.

One of the main goals of the exoplanet research is to find a new Earth. That is because the Earth is the only known planet with a life so far. Therefore scientists look for the Earth-like planets orbiting a Solar-type stars. The first exoplanet orbiting a main sequence star was discovered in 1995 by Michel Mayor and Didier Queloz of the University of Geneva (Mayor & Queloz 1995 [28]). In 1997 it was confirmed by another team (Marcy et al. 1997 [26]). The discovery was made using radial velocity measurements. Discovered exoplanet is a gas giant orbiting the star 51 Pegasi. It orbits its parent star at close orbit with semi-major axis only 0.0527 AU. This was quite unexpected as it was expected like in our Solar system that giant gas planets orbit stars at far orbits as in the Solar System. Close orbiting planets are extremely heated by its parent star, so these giants are called hot Jupiters.

In 1999 a transit of already known planet HD 209458 b was detected (Henry et al. 1999 [19], Charbonneau et al. 2000 [10]). It has confirmed previous discoveries. Having the exoplanet observed using two different methods (radial velocity measurements and photometry) it could be described in detail and approximate mass could have been calculated. In 2002 an atmosphere of the of HD 209458 b was detected (Charbonneau et al. 2002 [11]). It was the first detection of atmosphere on the exoplanet.

In the first years of 21st century tens of new extrasolar planets have been discovered. New methods have been used such as transit timing or transit duration variation (used for observing new planets in an already known systems; Agol & Fabrycky 2018 [2]), pulsar timing (Silvotti et al. 2007 [44]), gravitational microlensing (Beaulieu et al. 2016 [4]) or even direct imaging (Kuzuhara et al. 2013 [24]).

A significant progress has been made by using space telescopes. At first Hubble Space Telescope and Spitzer Space Telescope were used for the observations (Benedict et al. 2006 [5], Nutzman et al. 2009 [34]). Later in 2006 CoRoT space observatory was launched. It was the first mission primarily focused on the search for exoplanets using the method of transit photometry (Baglin et al. 2006 [3], Monteiro et al. 2006 [30]). Because of the technical problems, mission stopped operating in 2013. Despite of that it was a success with around 30 discovered exoplanets. CoRoT made a way for new more advanced space telescopes such as Kepler or TESS.

Kepler space telescope was launched in 2009 and it was operating until late 2018. Alike the CoRoT mission, Kepler was searching for the transiting exoplan-

ets via photometric method (Borucki 2016 [6]). Primary mission was planned for three and half years. The telescope was orbiting on the heliocentric orbit with semi-major axis similar to the Earth's. It was observing only one field of view for the whole time. Thanks to that it was collecting continuous photometric data of more than 170,000 stars simultaneously. In 2013 mission had to be changed because of the failure of two out of four reaction wheels. Kepler's second mission named "K2" started in 2014 and lasted until the telescope had run out of the fuel in October 2018. During the second mission, solar wind was used to stabilize the telescope at the orbit. Kepler was then able to observe one field of view for approximately 80 days. After that it's position had to be changed for another time interval.

Kepler/K2 mission was an enormous success. The telescope had observed more than 500,000 stars during nine years. It found more then 5,000 candidates and more than 3,000 of them have been confirmed so far as the exoplanets.

The only problem with the Kepler mission was that it was not suited for follow-up observations from the ground. To confirm the exoplanet candidates it is necessary to observe them at ground based observatories (Martin et al. 2019 [27], Furlan et al. 2017 [15]). For more detailed characterization (such as determining the mass of exoplanet) using other method — different then the photometric method is needed (such as radial velocity measurements). Many stars observed by Kepler were relatively faint stars (with magnitudes between approximately 9 mag and 16 mag. For precise radial velocity measurements the sample of targets for 2-meter telescopes is limited. That is the reason there are more unconfirmed or uncharacterised exoplanets than the planets fully characterized (by full characterization we mean the basic parameters are known such as mass, diameter and a density of the planet, orbit radius and inclination).

These findings were used for planning mission TESS (Transiting Exoplanet Survey Satellite). It targets the stars with apparent magnitudes brighter than $\sim 12 - 13$ mag (Ricker et al. 2015 [40]). Limit for the brightest stars is around magnitude 4 to 6. With this range of magnitudes follow-up observation are easier and more precise. Primarily targeted are stars of spectral types from F5 to M5 (Ricker et al. 2015 [40]). This criterion is used since it is easier to detect an Earth-sized planet near the dwarf stars and the main sequence stars. The rotation of young star or even the absence of spectral lines in its spectrum makes spectral analysis more difficult and not precise. Stars of the chosen types are also more likely to create habitable conditions for life on their planets, what makes them more interesting to study. Majority of exoplanets is expected to be found closer than 300 ly away from the Earth.

TESS has four CCD cameras with combined field of view (FOV) $24° \times 96°$ (Ricker et al. 2015 [40]). The ecliptic sphere is divided into 26 sectors with 13 of them on the northern ecliptic hemisphere and 13 sectors on the southern ecliptic hemisphere. One sector is observed for 27 days. then TESS moves to the other sector. Both north pole and south pole areas observed during each segments, since the sectors are overlapping there. This will allow to detect the long-period exoplanets.

1.1 Detection methods

1.1.1 Transit photometry

Transit photometry is one of the most effective methods for exoplanet research. It is an indirect method based on measuring the stellar brightness. If the planet passes in front of the stellar disk, a decrease in brightness can be observed. This phenomenon is called planetary transit. It can be observed only if the orbital plane lies in the line of sight from the Earth. Therefore, just a fraction of planets can be detected via this method. From the shape of the light curve a lot can be said about the planet — parameters such as an orbital period P and a distance from the star[1] a can be derived. Transit photometry can also provide an orbit inclination i, which is the key to calculating the mass of the planet M (Winn 2010 [54]).

A precise value of the planetary mass can be calculated only if combined with other methods (mostly Doppler spectroscopy). Transit photometry alone gives only an estimation of minimal mass of the planet m.

The period P is derived as a time between the two following transits. According to the Newton's gravitational law the semi-major axis can be calculated as (with the assumption planet mass is far less than mass of its parent star $M_\mathrm{p} \ll M_*$)

$$a^3 = \frac{GM_*}{4\pi} P^2 \,. \tag{1.1}$$

Luminosity drop of the star caused by the transit can be approximated to (Perryman 2000 [36])

$$\frac{\Delta L}{L_*} \simeq \left(\frac{R_\mathrm{p}}{R_*}\right)^2 = \delta \,, \tag{1.2}$$

where L_* stands for luminosity of the parent star, ΔL is the drop in luminosity and R_* (R_p) is the radius of the star (planet). The symbol δ stands for the transit depth. For this approximation we have to assume a uniform surface brightness of the parent star. For more precise calculations the effect of limb darkening[2] needs to be considered (Jacob et al. 2000 [20]). Using formula (1.2) a planet-to-star radius can be derived from the luminosity drop and so with the knowledge of the stellar parameters the planet radius can be calculated.

Transit duration can be derived as

$$\tau = \frac{P}{\pi} \left(\frac{R_* \cos d + R_\mathrm{p}}{a}\right) , \tag{1.3}$$

where d is the latitude of the transit on the stellar disk (as in Perryman 2000 [36]). Because the transit duration can be derived directly from the light curve, equation (1.3) can be used to calculate the parameter d.

[1] More exactly called semi-major axis.

[2] Decrease in the brightness can be observed on the edge of the stellar disk due to light passing through the thicker stellar atmosphere.

Finally the orbital inclination can be derived as

$$\cos i = \frac{R_* \sin d}{a} \,. \tag{1.4}$$

Thanks to the space telescopes — so far mostly Kepler — most of the exoplanets have been discovered with method of transit photometry. The method is so effective, because it is suitable as well for observing of a single star as for observing of the large stellar field at once. For example Kepler had FOV approximately $10° \times 10°$ (Van Cleve & Caldwell 2009 [52]) and TESS has FOV combined of four cameras $24° \times 96°$. Data are collected in parallel for all stars observed in the FOV for the whole observation which increases the probability of the detection of transit[3]. This is crucial for detecting of the Earth-sized planets orbiting the parent stars on the Earth-like orbits.

1.1.2 Radial velocity measurements

The Doppler spectroscopy is another indirect method widely used for exoplanet research (Bozza et al. 2016 [8]). As one of the spectroscopic methods it is based on the analysis of the spectrum of host star. An exoplanet influences its parents star with its gravity. That causes the star to orbit around the star-planet barycentre (it can be located under the stellar surface). This motion is rather small but often measurable (e.g. radial velocity amplitude of 51 Pegasi is approximately $100\,\mathrm{km{\cdot}s^{-1}}$ (Marcy et al. 1997 [26]). It is detected as a Doppler shift of the spectral lines in star spectrum. The effect is stronger for heavy planets. From the Doppler shift the radial velocities are derived in comparison to the radial velocity (RV) template.

There are several methods of what to use as a template for comparison (Bozza et al. 2016 [8]). We can use the spectrum of the RV standard star[4] which does not change its radial velocity. For the precise measurements it is effective to choose a star of the same spectral type as the target star. This is because of the similar spectra and the spectral lines to compare. Another option is to compare measured shift with the telluric lines in the (target) star spectrum (Griffin et al. 1973 [16], Guenther et al. 2003 [17]). Telluric lines are the spectral features caused by water vapour in the Earth's atmosphere. Molecules in the atmosphere absorb and emit their own light which contaminates the detected star spectrum. This effect can be used since the position of telluric lines in the spectrum is stable independently on the star spectrum.

For the RV measurements only the position (shift respectively) of the spectral line is necessary. We are interested in the relative change of RVs, therefore, one can choose the template frame (e.g. chosen according to the best signal-to-noise ration) from the time series acquired for the target. The same method was used for data processing in this thesis. Intensity or shape of the spectral lines is not important, but it can affect the precission. In some cases the result RV can be changed (Fischer et al. 2016 [14], Dupkala 2018 [13]). Obviously a high signal to noise ration is important for accurate measurements.

[3]More systems observed at once means more likely one is in a good geometry for the transit detection

[4]There are several catalogues of the RV standards, e.g. Geneva Radial Velocity Standard Stars (`http://obswww.unige.ch/~udry/std/std.html`).

The amplitude K of radial velocities can confirm whether the candidate is the exoplanet or just a false positive — if the amplitude is too high, mass of the object causing the stellar movement has to be too big for a planet (it appears as an object with the stellar-like mass). Eclipsing binaries are the most common origins of the false positives[5]. Orbital period P and eccentricity e can be computed from the radial velocity curve and its shape. With the knowledge of the host star mass M_* radial velocity amplitude can be expressed as

$$K = \left(\frac{2\pi G}{P}\right)^{\frac{1}{3}} \frac{M_\mathrm{p} \sin i}{(M_\mathrm{p} + M_*)^{\frac{2}{3}}} \frac{1}{(1-e^2)^{\frac{1}{2}}}\,, \tag{1.5}$$

where $M_\mathrm{p} \sin i$ is the mass of the exoplanet (Perryman 2000 [36]). Therefore the orbital inclination is necessary for determining the planetary mass. This shows why the Doppler spectroscopy combined with the method of transit photometry is so useful (otherwise just the lower mass limit can be derived).

Before the launch of Kepler, method of radial velocity measurements was the most effective method for discovering the exoplanets. Nowadays it is often used for follow up observations of exoplanet candidates thanks to the all parameters it can provide. However, the radial velocities are not the only useful information which can be derived from the stellar spectra. Chemical composition, existence of the exo-atmosphere and other characteristics can be derived from the spectra as well (Sing et al. 2016 [45]). It is also used for star characterization (as have been stated before it is necessary for the calculation of exoplanet parameters, Pepe et al 2014 [35]).

Rossiter-McLaughlin effect

For the Doppler analysis it is not necessary for the exoplanet to transit the star. However, if the exoplanet is transiting and the spectrum is taken during the transit, additional information about the planet can be determined.

As the star is rotating, one quadrant of its disk is moving towards the observer and the other one is moving away from him. Because of that, "approaching" quadrant produces the blue shift while the one moving away produces the red shift in the stellar spectrum. Basically it can be observed as a broadening of the spectral lines in the stellar spectrum. Transiting exoplanet covers different portions of the stellar disk with different average radial velocities. This causes the anomalies in radial velocity curve which can be detected (as shown in Figure 1.1). It is called the Rossiter-McLaughlin effect (Boué et al. 2013 [7]). Two papers published by Rossiter (1924) [41] and McLaughlin (1924) [29] gave the name to the effect.

The effect is important for calculating the angle between the stellar spin-axis and the orbit of the planet (hereafter spin-orbit angle). From the shape of the Rossiter-McLaughlin effect (RM effect) important characteristics can be derived, such as the planet-star size ratio, the rotational speed of the star or the impact parameter. It also gives information about the orbital inclination or the rotational spin directions of the exoplanets. The RM effects can be used for

[5]Another origin might be the brown dwarfs. The radial velocity method is useful for characterization and further studying of brown dwarfs and eclipsing binaries as well as for the exoplanets (Guenther et al. 2003 [17]).

determining an atmospheric composition or in search for exo-moons[6] (Triaud 2018 [51]). Nowadays, it is a standard procedure to determine the RM effect as the stellar spectra are studied.

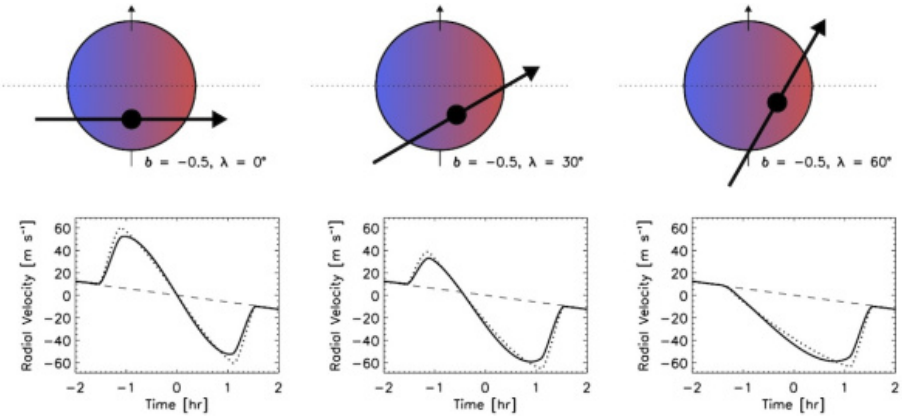

Figure 1.1: Illustration of the Rossiter-McLaughlin effect for three exoplanets: WASP-66b, WASP-87b and WASP-103b. The color on the star disk corresponds to the radial velocities of the various parts of the surface. Image taken from [53] based on the results of Addison et al. 2018 [1].

[6]Exo-moons are natural satellites of the exoplanets as the Earth's Moon. So far no exo-moon has been sufficiently detected.

2. The instrumentation

All the data used in this thesis were acquired using the Perek telescope at Astronomical institute of the Czech Academy of Sciences in Ondřejov. The telescope is operated by the Stellar department. It was built in 1967[1] (web pages of the Stellar dept. of AI CAS [48]). With 2 meter primary mirror the telescope falls into category of smaller meter-sized telescopes. It is used only for spectroscopic observations. Firstly, the photographic plates were used as the detection element for spectra exposition. Since 1992 the electronic detectors have been used. A Reticon detector was used until 2000 when it was changed for CCD chips. Currently the telescope is equipped with two spectrographs — a single order coude spectrograph (used in two configurations — with CCD400 or CCD700 camera) and the echelle spectrograph.

A basic difference between the single order and the echelle spectrograph is that echelle spectrograph creates many narrow orders while the single order spectrograph works in two spectral orders. Because the echelle orders are overlapping it is possible to merge them into one continuous spectrum. The resulting spectrum covers a large wavelength region (it might cover more then just a visible light).

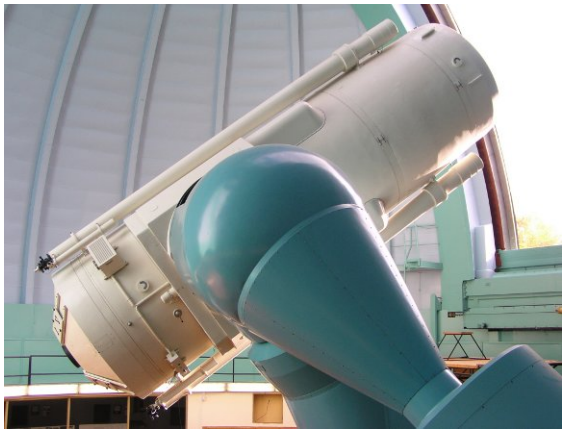

Figure 2.1: Perek 2-meter telescope at Ondřejov observatory. Picture taken from the web pages of the Stellar dept. of AI CAS [48].

2.1 Perek telescope

The Perek telescope (Figure 2.1) is a coude system on a special equatorial mount[2] (web pages of the Stellar dept. of AI CAS [48]). Its main optical element is a parabolical mirror with effective diameter 2 meters and a focal ratio 1:4.5 (focal length is 9 meters; Šlechta & Škoda 2002 [47]). The secondary mirror is a convex hyperbolical mirror with effective diameter 0.58 meters. Its focal ratio is 1:32.

[1]The telescope was built thanks to initiative of a Czech astronomer Luboš Perek. For his credits it was named after him in 2012.

[2]Two other configurations of the telescope are possible — the Cassegrain system or using of the primary focus. However, only the coude system is used.

There are also two flat mirrors used for guiding the light and a splitting plate, which divides the environment in coude room and the dome.

In coude system the star light goes first to the primary mirror, which reflects it to the secondary mirror. From there it goes to the first flat mirror which sends the light out of the telescope tube into the mount (this is a specific sign of a coude system). In the mount there is the second flat mirror which reflects the light once again. It guides the light down through the mount to the splitting plate. From the splitting plane the light continues to the coude focus, which is located in lower level under the telescope. The effective focal length of the coude system is 63.5 meters.

The telescope is operated from the control room which is located under its mount. The targets are chosen from the database and the coordinates are then sent to the telescope guidance system. The data in the database are taken from the SIMBAD[3] database.

2.2 Ondřejov Echelle Spectrograph

Ondřejov Echelle Spectrograph (hereafter OES) was used for obtaining of all the spectra collected in our observation campaign. OES was installed at the observatory in 2004 but until 2013 it was used only exceptionally. Since 2015 it is systematically used for exoplanet follow-up observations.

Scheme of the OES is shown on Figure 2.2 (Šlechta [46]). Technical parameters of the device are described in Koubsky et al. 2004 [23]. There is a slit located in the coude focus. Placing the slit in the focus creates sharp and focused spectrum. The light continues from the slit to the first collimator which collimates the light beam to the echelle grating. The collimator has the shape of a spherical mirror with focal length of 4637 mm and f/32. It produces a beam of 142 mm in diameter. The echelle grating with the blaze angle of 69 ° has the dimensions $420 \times 165 \times 74$mm. Since its edges are 4 mm thick the optically active area is a little smaller. The grating's groove density is $54.5\,\mathrm{g \cdot mm^{-1}}$ and it was manufactured by The Richardson Grating Laboratory (formerly part of Milton Roy Company).

The intermediate spectrum is created by the grating. At first it is imaged with an f/36 parabolic mirror (also called as camera mirror). Its focal length is 1628 mm. The mirror is partially cut from both sides. The reason for this is that the uncut mirror would be blocking the light beam which is led next to it. From there the light goes to a small flat mirror (it is used as an optically neutral just for the breaking the path of light). There the light is reflected to the secondary collimator. It has the parabolic shape with focal length of 1086 mm and f/3.1. The second collimator is the place where a "white pupil" in parallel light is formed. That is the white image of the echelle grating reduced from 142 mm to 95 mm in a diameter. Then the light goes to the crossdisperser — a 54.5 ° LF5 prism. It divides the echelle orders so in the camera focus it cover the area of 30×10.5mm. The crossdisperser is placed in front of a CANON EF 200 f/1.8 camera lens with a focal length of 200 mm. The distance between the chip and the crossdispersing prism is only 1 mm.

[3]SIMBAD, Centre de données astronomiques de Strasbourg (`http://simbad.u-strasbg.fr/simbad/`)

For the detection of spectra a CCD chip is used (an EEV 2048 × 2048 pixels array with pixels size 13.5 μm). The chip is a Versarray 2048B system (Roper Scientific). For cooling of the chip a dewar filled with a liquid nitrogen is used. The chip is connected to a controller which is located within its setup. Orders on a detected spectrum are divided with a distance from 12 pixels in the red end to 27 pixels in the blue end of the spectrum. The result orders are also curved and in the red end of the spectra they are not entirely overlapping. These effects need to be corrected within the data reduction (we will describe it later in chapter 4). The slit width defines the resolution of the spectrograph, when set to 600 μm the resolution is 51600 at 5000 A. The spectral range is approximately from 3700 to 9000 A.

The OES spectrograph is located in the room under the telescope. The space is partially isolated. However, a technician has to go to the spectrograph room everyday to refill a liquid nitrogen into the cooling system of the camera. Therefore, there is a heat exchange between the OES room and the hall connecting it with the control room. As the liquid nitrogen is vaporizing in time, temperature of the camera can be also changing a little. The liquid nitrogen refilling is usually done from a half hour to a few hours before the observation starts. The tests have proved this factor does not have a significant influence on the result radial velocities if the precision is no more hundreds of meters per second. For more precise RV measurements on the level of ones or tens of meters per second the heat exchange and the liquid nitrogen vaporization may influence the results. Since our results have the accuracy around a few hundreds of meters per second, we did not consider this effect (Kabáth et al. 2019 [21] and Kabáth et al. 2019 [22]).

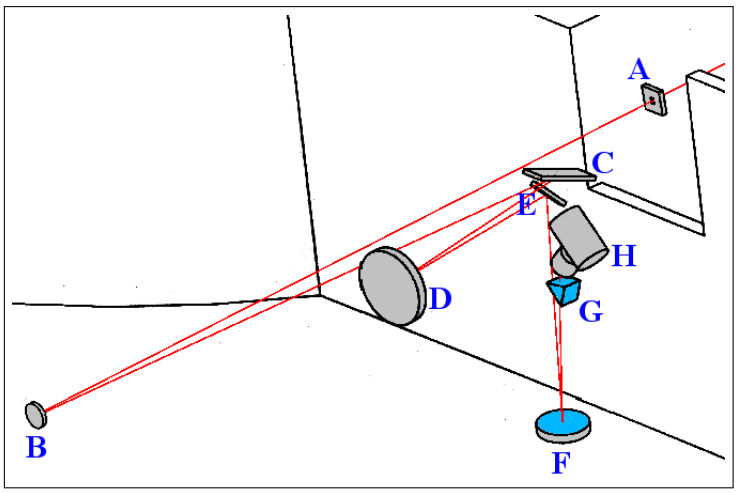

Figure 2.2: Scheme of the OES spectrograph. **A** The slit, **B** first collimator, **C** echelle grating, **D** parabolic mirror, **E** small flat mirror, **F** secondary colimator, **G** crossdisperser, **H** camera with the CCD chip (Šlechta [46]).

3. Observational data set

We observed an A-type star HD 185603 with a known transiting exoplanet MASCARA-2b or KELT-20b respectively. The exoplanet discovery was announced by Lund et al. (2017) [25] and later it was confirmed by Talens et al. (2018) [50].

As an exoplanet candidate, MASCARA-2b was found using Kilodegree Extremely Little Telescope (KELT) in KELT-North field 11. For the photometric follow-up observations the KELT Follow-Up Network (KELT-FUN) was used. It includes the observations from several observatories. To confirm the discovery, a high contrast adaptive optics (AO) imaging and the spectroscopic follow-up observations were done as well. The star was also observed using MASCARA system with additional photometric and spectroscopic follow-up observations.

MASCARA-2b is a hot Jupiter with short orbital period. It is orbiting a main sequence star. Both parent star and exoplanet parameters are listed in Table 3.1 and Table 3.2 respectively.

Parameter	Symbol	Unit	Value	Ref.
Right Ascension	RA		19 38 38.73	1
Declination	DE		+31 13 09.21	1
V-band magnitude	m_V		7.58	1
Spectral Type			A2V	2
Parallax	π	mas	7.41 ± 0.39	2
Stellar mass	M_*	$M_\odot$	1.89 ± 0.06	3
Stellar radius	R_*	$R_\odot$	1.60 ± 0.06	3
Effective temperature	T_{eff}	K	8980 ± 130	3
Projected rotation speed	$v \sin i_*$	$\mathrm{km \cdot s^{-1}}$	114 ± 3	3

Table 3.1: Basic parameters of HD 185603. References: [1]SIMBAD Database [18], [2]Lund et al. 2017 [25], [3]Talens et al. 2018 [50]

Parameter	Symbol	Unit	Lund et al. 2017	Talens et al. 2018
Epoch	T_0	BJD	$2\,457\,485.749\,65 \pm 0.000\,20$	$2\,457\,909.5906 \pm 0.0003$
Orbital period	P	h	$3.474\,108\,5 \pm 0.000\,001\,9$	$3.474\,199 \pm 0.000\,006$
Transit duration	T_{14}	h	3.57 ± 0.03	3.55 ± 0.03
Transit depth	δ	-	$0.013\,06 \pm 0.000\,14$	0.013
Planet-to-star ratio	R_p/R_*	-	$0.114\,26 \pm 0.000\,62$	0.115 ± 0.001
Inclination	i	$^\circ$	86.15 ± 0.28	86.4 ± 0.5
Impact parameter	b	-	0.500 ± 0.029	0.47 ± 0.06
Semi-major axis	a	AU	0.0542 ± 0.0021	0.057 ± 0.006
Planet radius	R_p	$\mathrm{R_J}$	1.735 ± 0.075	1.83 ± 0.07
Planet mass[a]	M_p	$\mathrm{M_J}$	< 3.518	< 17
Equil. temperature	T_{eq}	K	2261 ± 73	2260 ± 50

Table 3.2: Planet parameters of MASCARA-2b. Compared values taken from two different papers (Lund et at. 2017 [25] & Talens et al. 2018 [50]). [a]3σ mass limit.

3.1 Target selection

The target for the observations was selected according to several criteria. As one of the objectives is to explore the suitability of the Perek telescope and OES spectrograph for TESS follow-up observations, the target was chosen as a star similar to those targeted by the mission. Therefore only relatively bright stars were considered. The observation limits of the telescope and the spectrograph were also taken into account Using the telescope, suitable SNR can be obtained for stars brighter than 9 mag. For the continuous observations the target star has to be visible for the sufficient period of time. Given the location of the observatory stars at the southern sky hemisphere were excluded from the survey.

Since we focused on the transiting exoplanets (or candidates), we were looking for a star with known (or predicted) transiting exoplanet in order to further study the system. Especially we were interested in exoplanets with known exo-atmosphere features (Nortmann et al. 2018 [33]).

3.2 Data set

We observed MASCARA-2b during 28 nights from March to October 2018 and we obtained 211 spectra in sum. All the observations are listed in Table 3.3. For the majority of nights only a few spectra were taken. Beside that we conducted 8 full-night observing campaigns and 5 of them were observed during the transit (shown in Table 3.3). As a result we have 100 spectra taken during the transit.

The images were taken with exposure times 1800 or 600 seconds. Shorter exposure time was used especially for transit observation campaigns. The purpose was to take images with a small time step to obtain more spectra during the transit. Shorter exposure was done at the cost of lower SNR. As discussed later in chapter 5 this decrease in SNR was not optimal for precise RV measurements. The read-out time between two following images is 43 seconds. An example raw echelle spectrum of MASCARA-2 is shown on Figure 3.1.

From the nights available for observations according to the telescope schedule the observation nights were primarily chosen according to the orbital phase of MASCARA-2b. Transit nights had the biggest priority. Except for them observations were planned in order to cover different orbital phases. Full-night campaigns were combined with a routine observations when 2 to 4 images were taken.

The observations are limited by the weather condition. For spectroscopic observation the requirements are not so strict as for the transit photometry. Mostly clear sky is needed. However, it is not a problem to interrupt the observation for a short period of time. Another important factor is the humidity. It is not possible to conduct the observation when relative humidity is 90% or more for the safety reasons[1]. This is a problem especially in spring and fall season.

Star altitude had to be taken in consideration as well. The typical limit of altitude above the horizon of the target is 20 °. Given a good celestial position of MASCARA-2 (located in Cygnus constellation) this parameter did not influence

[1]When the relative humidity is higher than 90% the risk of a condensation is to high. Condensation of water vapor on the telescope mirror could cause a decrease in its reflectivity.

the observations in spring and summer season. In September the target star was higher than 20° above the horizon for most of the night. In late October the observation was possible for the first half of night.

No.	Night	Spectra	Exposure time (s)	Template	Notes
1	2018-03-21	2	1800	1	
2	2018-03-25	1	600	1	
3	2018-04-11	1	1800	1	
4	2018-04-14	1	1800	1	
5	2018-04-17	1	1800	1	
6	2018-04-18	1	1800	1	
7	2018-05-18	3	1800	2	
8	2018-05-19	3	1800	2	
9	2018-05-26	2	1800	2	
10	2018-05-28	4	1800	2	
11	2018-05-30	4	1800	2	
12	2018-07-14	7	600	3	
13	2018-07-15	2	600	3	
14	2018-07-18	2	1200	3	
15	2018-07-19	24	600	3	transit campaign
16	2018-07-20	4	600	3	
17	2018-07-26	16	600	3	transit campaign
18	2018-08-03	3	600	3	
19	2018-08-16	16	600	4	transit campaign
20	2018-08-17	17	600	4	
21	2018-08-20	13	600	4	
22	2018-08-26	16	600	4	transit campaign
23	2018-08-29	16	600	4	
24	2018-09-04	6	600	4	
25	2018-10-11	6	600	5	
26	2018-10-17	6	600	5	
27	2018-10-18	6	600	5	
28	2018-10-21	28	600	5	transit campaign

Table 3.3: MASCARA-2b data set. Table shows date and number of spectra obtained during the observation.

3.3 Correction frames

For the data reduction various correction frames are necessary to remove the imperfections such as different pixel sensitivity, cosmic ray hits, bad pixels etc. They are taken within every observation run. The set of correction frame consists of 10× bias frames, 10× flat lamp frames and 4 to 6× comparative images.

Bias frames

Bias frames (also called zero frames, Figure 3.3) are images taken with zero exposure time. Bias frames are used for removing of the readout signal detected from the camera sensor. A median image of 10 images is used.

Flat frames

Flat lamp images (Figure 3.5) are used for correction of different pixel sensitivity of the camera sensor and the imperfections in the optical path of the light. Flats are the images of homogeneously illuminated surface. They can be acquired as dome flats using white illuminated screen in the dome or lamp flats using an internal calibration lamp, what was the method we used. As for the bias frames a median frame of 10 flat frames is used for reduction. Exposure time of a single flat field is 40 seconds.

ThAr comparison spectrum

Image of the Thorium-Argon comparison spectrum (hereafter comps, Figure 3.4) are necessary in the process of identifying the spectral lines in the star spectra (the method is described in detail in chapter 4). Thorium-argon lamp is used as the light source. ThAr lines are known with very high accuracy and so they can be used for spectral lines identification of the science images. The comps (also called arc images) are taken in the series of 5 to 6 two times per night. All of them are taken in a row because of the heating of ThAr lamp — the lamp is unstable after switching it on before the heating stabilizes.... This takes about $10 - 15$ minutes. The exposure time of comp image is 140 seconds. Usually only the last (the best) image is used for the reduction.

Dark frames

Dark frames are used for the reduction of the thermal noise. We did not take any dark frames because, as was shown earlier, it does not have any significant effect on the data nor the results (Dvořáková 2018 [12]).

Template for aperture definition

Template for aperture definition is usually a bright star with the light intensity high on a wide spectral range is chosen. For our data set we chose Vega (alpha Lyrae) as an aperture template (Figure 3.6). Each night two spectra of Vega were taken with exposure times from 30 to 120 seconds depending on the weather conditions, mainly seeing and sky transparency.

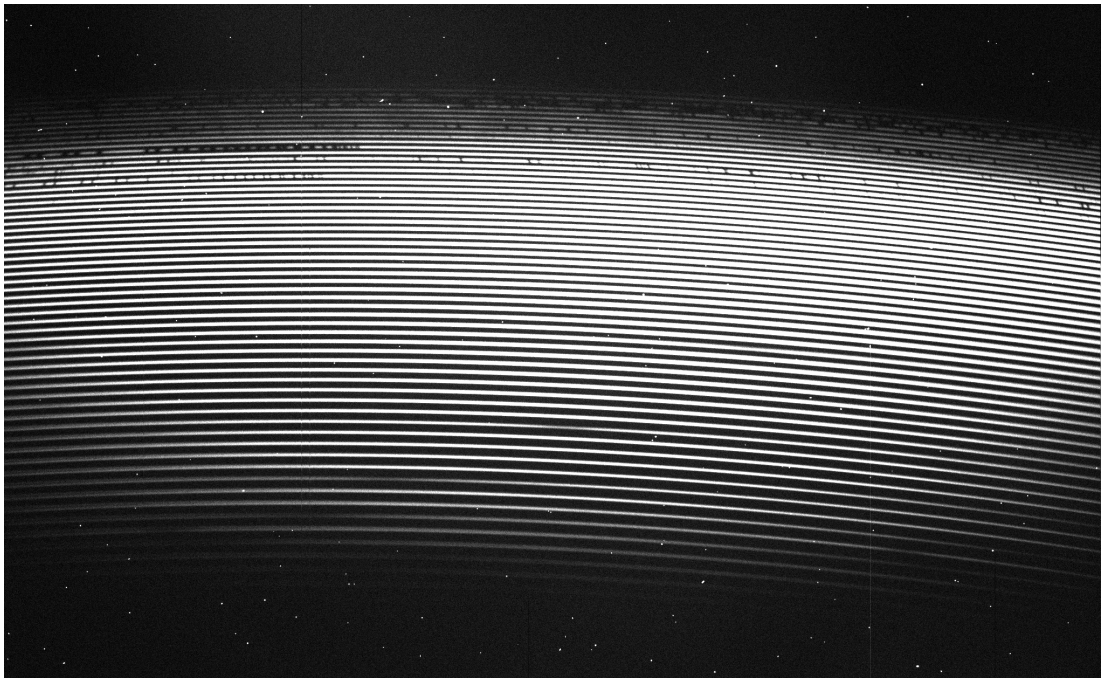

Figure 3.1: MASCARA-2, raw image (taken 2018-04-11, exposure time 1800 s).

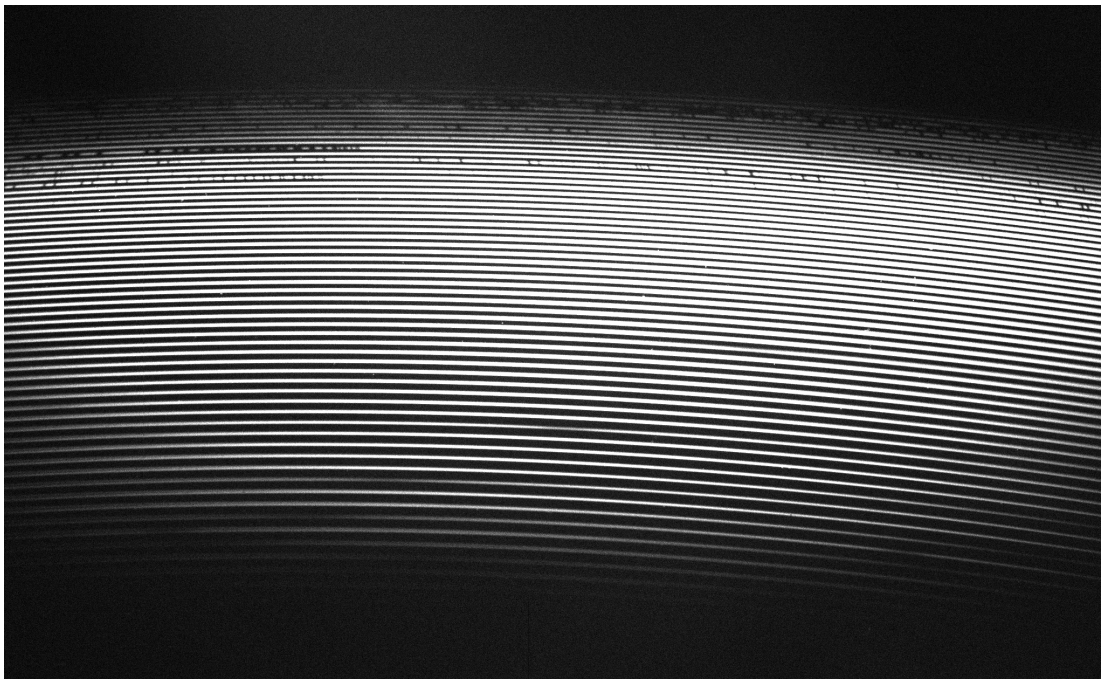

Figure 3.2: MASCARA-2, image with cosmic rays removed, bias, flat and bad pixels correction (taken 2018-04-11, exposure time 1800 s).

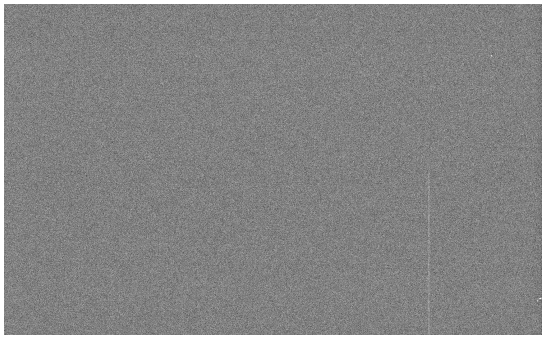

Figure 3.3: Bias correction frame (raw image, taken 2018-04-11, exposure time 0 seconds).

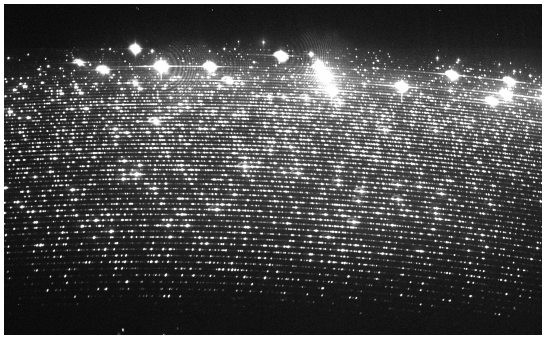

Figure 3.4: Th-Ar comparison frame (raw image, taken 2018-04-11, exposure time 140 seconds).

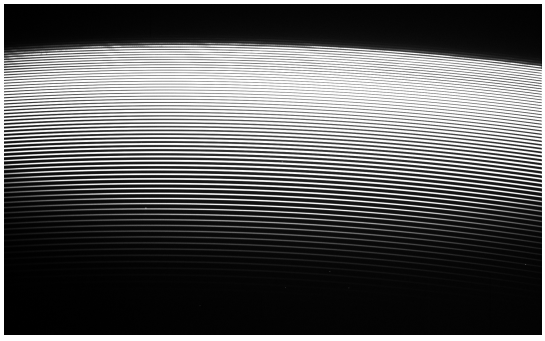

Figure 3.5: Flat lamp correction frame (raw image, taken 2018-04-11, exposure time 40 seconds).

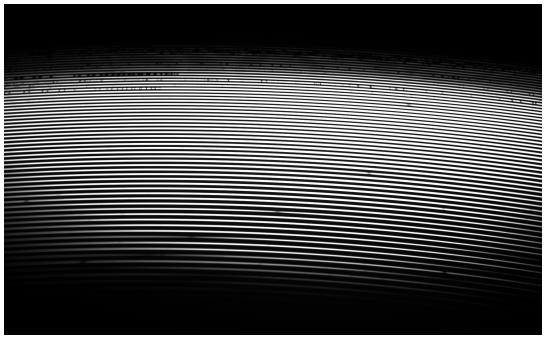

Figure 3.6: Vega (alp Lyr), aperture template frame (raw image, taken 2018-04-11, exposure time 120 seconds).

4. Data reduction

Raw data are saved on the servers of AI CAS. Before the reduction, a data set needs to be downloaded and sorted. It is ran by the shell script which does the sorting. The script also adds several information into image headers, such as name of the object or image type (bias, flat etc.). Julian date (JD) is written into the header as well. This parameter is necessary for the RV determination.

For all the data processing (spectra reduction, extraction and RV determination) IRAF software[1] is used. In the process science images (in this case images of MASCARA-2), bias images, flat images and comps (comparison images) are used. As stated in chapter 3 usually only the last comp is used as it is the best one (because of the gradual heating of ThAr lamp). The template spectra (as described in chapter 3 Vega is used for the aperture template) are included in science images.

4.1 Image reduction

The reduction process starts with the cosmic rays removing. Since the spectra are exposed for 600 seconds and more, cosmic rays are significantly detected on the images. For removing of comsic rays two procedures are used. As the first one a DCR algorithm[2] is used (Pych 2004 [39]). It is applied on all frames except comp. It is because the algorithm is not working correctly on the comparison images. Since their exposure time is only 140 seconds it is not a problem as there are only a few cosmic rays detected during the exposition. This method could be also applied for other images with a short exposure (bias and flat images). Nonetheless in their case it is working correctly and so the program is used.

After using the DCR algorithm, all frames (even comp) are corrected of bad pixels with an IRAF task *fixpix*. A special bad pixel mask adapted for OES spectra is used. Right after that the task *cosmicrays* is applied. It is the second method for removing of the cosmic rays in the pipeline. Comparison image is excluded once again.

The spectral orders do not cover the whole frame. On the vertical axis (y-axis) the bottom and the top of the frame is empty and therefore it is cut off. On the left and right edges of the frame the orders are curved. This may influence further processing and aperture identification. To avoid it a small part of the frame is cut off on the horizontal axis as well. Task *imcopy* is used for cutting. As the result in x-axis used pixel range is 5 to 2039 and in y-axis pixels 500 to 1749 are left for the further processing. This procedure is applied on the whole data set.

In the next step a masterbias frame is created as the median value of all bias frames (in our case it is most usually 10 images). It is done with *zerocombine* task. Then the flat frames are reduced of the masterbias frame using a simple

[1] National Optical Astronomy Observatory, `http://ast.noao.edu/data/software` (retrieved on 2018-05-04).

[2] It is possible to freely download the DCR program [39] from `https://users.camk.edu.pl/pych/DCR/` (retrieved on 2018-05-04).

imarith task operation. Reduced flat frames are combined to the masterflat frame (as a median frame of all flat images).

The next step in the reduction process is to create a template frame for definition of apertures (i.e. echelle orders, see Figure 4.1). When the template is created it can be used for aperture definition of images from several nights. The stability of the echelle orders is slightly changing in time. Therefore, one template can be used for data taken in less then a month, interval of two weeks is ideal. For the template spectrum with high SNR and well defined lines is chosen.

Chosen template frames are listed in Table 4.1. Template numbers correspond with template in Table 3.3 which was used for reduction data from chosen night. For sufficient stability we used one template for data from three weeks on average.

Date	Template number	Exposure time (s)	RMS
2018-04-11	1	120	0.0019
2018-05-26	2	30	0.0019
2018-07-20	3	30	0.0018
2018-08-20	4	30	0.0019
2018-10-17	5	30	0.0019

Table 4.1: Template frames used for aperture definition. Vega (alp Lyr) was used as a reference star. Template numbers correspond to the templates in Table 3.3. RMS value shows an accuracy of the wavelength solution for ThAr spectral lines identification.

For the aperture definition the *apall* task is used. In the OES spectra 56 orders are identified. The Chebyshev polynomial function of the first order is used for fitting. It is done automatically and then check in the interactive mode. If the apertures are not fit precisely it is corrected with Gaussian fit. The apertures are also corrected individually. Sometimes it is necessary to remove the outliers.

The image with already identified apertures is then used as the template for other spectra. Firstly, masterflat frame is normalized using the template and the result is normalized masterflat. For this operation the *apflatten* task is used.

After all the correction master frames are prepared, they are used for reduction of the comparison frame and sciences images (through the *imarith* operations). ThAr comparison frame is reduced of masterbias and then normalized with the normalized masterflat frame. Science images are reduced in the same order.

Using *apall* once again apertures of the science images are identified according to the template frame.

For the aperture definition of comp frame the apertures are cut (the space between the orders is thrown away). To gain a better accuracy for each science image a 'special' comp with extracted apertures is created. Science images are used as templates for the aperture definition of the original comp (in *apall* task) which results to the set of 'specialized' comps[3].

[3]When there are 4 science images, 4 'specialized' comps with extracted apertures are created from the originally used comp frame.

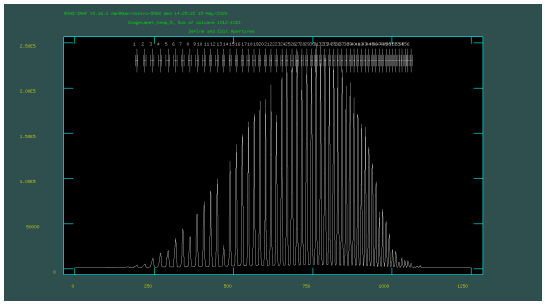

Figure 4.1: Aperture definition using the *apall* task. Vega is used as the template spectrum, exposure 30 seconds, 2018-08-20.

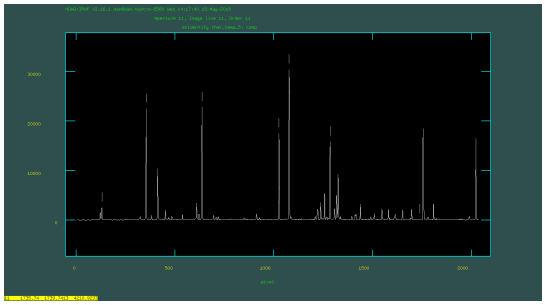

Figure 4.2: Spectral line identification using the *ecidentify* task. Identification is done on ThAr comparison spectrum from 2018-08-20.

4.2 Spectra identification

The next part of the reduction process is the spectral lines identification. It is based on comparing of the spectral line of a known spectrum — in this case spectrum of the ThAr lamp.

For simplifying of the process, a ThAr template frame is chosen from the data set. The known spectral lines are identified in order to get a reference wavelength solution. It is then used for reidentification of other spectra in chosen time interval. The templates we used for the primary identification are the 'special' comp images of the aperture template frames (created in the previous step). As the aperture templates have significantly better SNR than the science images, we gain a higher accuracy when using them for creating the 'special' comps used as the ThAr templates. ThAr comparison frames were taken from the same data set as the aperture templates (Table 4.1) and they were used for the same time intervals as well (Table 3.3).

For the spectral line identification, an IRAF task *ecidentify* is used (Figure 4.2). More than 100 most significant lines are manually identified according to ThAr lamp spectral lines catalogue. Then a line list can be used for automatic identification of the additional lines. There are 2000 lines on the list. A wavelength solution is found after using a Chebyshev function for the fit. Several outliers have to be removed and the fit is repeated. This process is repeated (usually 2-3 repetitions) until all the outlier are removed and the wavelength solution is sufficiently precise with RMS under 0.002 (RMS of the wavelength solutions for all ThAr templates is listed in Table 4.1).

After the wavelength function is found for the ThAr template it is used for reidentification (*ecreidentification* task) of other comps. Then they are assigned to the corresponding science images as the reference spectra (*refspectra* task) and the correct wavelength scale is assigned using the *dispcor* task (it uses the relation found from the comp versus science image overlay frames). The results are the spectra in a wavelength scale (so far the spectra were in a pixel scale). However, the spectra are still divided into 56 orders an they are not normalized.

With the task *continuum* each single order is fitted (Legendre function is used for the fit). The the orders are divided by their fits (task *sarith* to get the 1-dimensional (1D) spectra (the orders are straighten up). Both 1D single orders and their fits are then merged into one spectra and fits respectively. For merging

the *scombine* task is used. 1D spectra are divided by the merged fits once again to be normalized.

The last part of the data reduction is removing of the regions where the orders are not overlapping due to design of the spectrograph. The shell script is used for setting the value in this regions to 1 (thanks that it does have less significant influence on the RV measurements). The spectra header is updated as well (parameters such as an exposure time).

Result of the data reduction is 1D normalized spectrum. Example spectra are shown on figures 4.3 (Vega), 4.4 and 4.5 (MASCARA-2).

4.3 Radial velocity determination

Determining of the radial velocities is precedes by several shift corrections in the stellar spectra.

4.3.1 Telluric lines correction

The first is the telluric shift correction. As described in chapter 1, telluric spectral lines do not change their position in the stellar spectra as they are due to water absorption in the atmosphere (actually they show a small movement but are stable down to approx. $20\,\mathrm{m\cdot s^{-1}}$ in ideal case; Griffin et al. 1973 [16]). Therefore, when there is a shift detected in their position it is a systematic error caused by the instrument. The spectra are shifted for the correction so the telluric lines are overlapping. Spectrum with the best SNR (one of the data set acquired on given night) is chosen as a telluric lines template. Radial velocities are then determined as the velocities relative to this template. nude teen

4.3.2 Telluric lines shift

For the telluric line shift determination an IRAF task *fxcor* is used. The shift is derived from a narrow region were the telluric lines are intensive, wide enough and stable. We used the region from 5917 A to 5926 A. For the correlation fit we chose the Gaussian function. Width of fitting region (of the one spectral line) was 30 pixels as well as the maximum width parameter. Resulting shifts were used as an input for the *dopcor* task which was used for shifting the spectra.

4.3.3 Heliocentric correction

After the telluric correction a heliocentric velocity[4] is derived and written into the spectra header. It is done with task *rvcorrect*. As the heliocentric velocity is determined for every spectrum, it is used for the heliocentric correction of the spectral shift (correction related to the Earth's movement around the Sun). Once again we used the *dopcor* task to shift the spectra.

[4]Generally it includes several radial velocity corrections related to the observer's movement. For this purpose the exact coordinates of the observatory are used.

4.3.4 Template for cross-correlation

With the heliocentric correction done, everything is prepared for the actual RV determination. Fitting parameters in *fxcor* task were the same as for the telluric correction except for parameters of fitting region width and maximum width, which are set to 100 pixels. The cross-correlation of template spectrum (hereafter radial velocity template) and the science image spectra is done on a different interval as well. Interval selection is described in chapter 5.

As the radial velocity template we used the same spectrum as for the telluric lines (although this is not necessary). It is corrected of the telluric lines shift and the heliocentric correction is done as well.

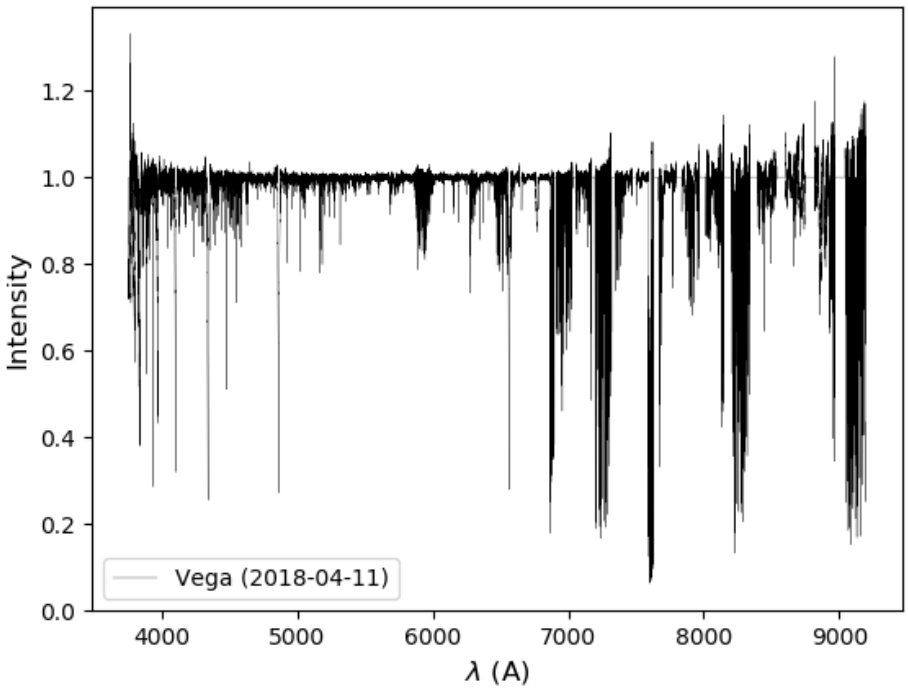

Figure 4.3: Reduced spectrum of Vega from 2018-04-11, exposure 120 s.

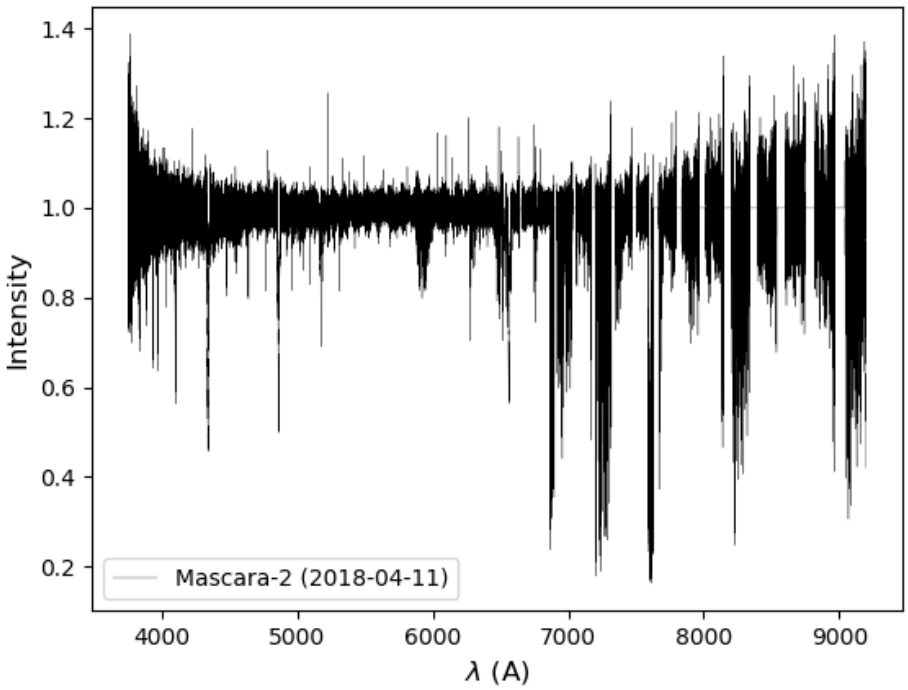

Figure 4.4: Reduced spectrum of MASCARA-2 from 2018-04-11, exposure 1800 s.

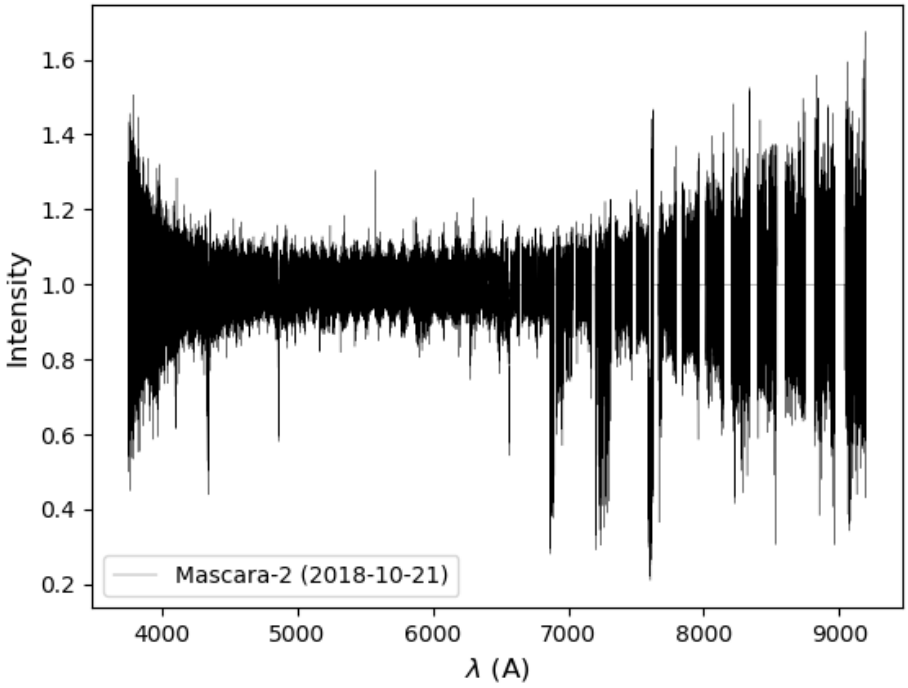

Figure 4.5: Reduced spectrum of MASCARA-2 from 2018-10-21, exposure 600 s.

5. Results

To get the best accuracy we tested several regions of spectra for the cross-correlation. At first we used *fxcor* task for deriving the RVs from the single interval of 4900 − 5400A. This was used in the previous analyses (Dupkala 2018 [13]) as the most stable region. It is not stable for MASCARA-2 as it is the star of a different spectral type. However, it was chosen because of the absence of telluric lines, which are significant in the red part of spectrum. We also tried to avoid any wide spectral lines which affect the cross-correlation. Intensive and wide lines (e.g. Hβ at 4861 A) are more significant then other spectral lines what causes errors when fitting is done on the whole region.

However, for many spectra the fit did not converge. Mostly it was because of the lower SNR. MASCARA-2 (as an A-type star) has less spectral lines in its spectrum, what influences the fitting as well. Therefore, we tried to fit just the single lines. We used the narrow interval around Hβ line. The results were similar as the fit often did not converge.

We tested several other regions. The one between 4900 and 6300 A was finally chosen as the best one. This region covers e.g. the Sodium D-lines and some ionized metals. For better accuracy and for elimination of deviations we did not apply *fxcor* on the whole interval but we divided it into 10 overlapping intervals of 500 A. The final RV is then calculated as an average of ten values for each interval. The errors are calculated as the standard deviations of these final RVs divided by the square root of number of the intervals (see the Formula (5.1)) . In some cases when the fit did not converge on the interval, it was not included in the final value, as well as the outlier values. With this method we gain an average precision of $\sim 0.3\,\mathrm{km\cdot s^{-1}}$ per one night when SNR is approximately 35 (corresponding to the images taken with exposure 600 s). We consider this to be the limit for given SNR. Since there are less than 7% of all frames taken with exposure time 1800 s, most of the spectra have similar SNR 35 ± 10. Therefore we used the described approach for all data (individual spectra alike full-night campaigns).

$$s = \frac{1}{\sqrt{N}} \sqrt{\frac{1}{N-1} \sum_{i=1}^{N} (x_i - \overline{x})^2} \tag{5.1}$$

5.1 Basic radial velocity measurements

For determining of the radial velocity curve we took all the data. The relative radial velocities were determined according to the template taken 2018-04-11. It was chosen because of the high SNR 43 (thanks to the longer exposure time of 1800 s). However, we could not create a relevant RV curve because of the systematic shift in the resulting RVs. As can be seen on Figure 5.1, the shift is increasing in time. A phase diagram affected by the shift can be seen on Figure 5.2.

We did the same analysis with another templates (from different nights with different exposure) but the results were affected by the systematic error as well.

Therefore we can rule out that the problem is caused by the RV template spectrum.

Generally, the shift does not occur in data acquired with the OES (Sabotta et al. *submitted* 2019 [42]). Nature of the instrumental shift will be investigated in more thorough analysis later.

5.2 Transit observations

The shift described in the previous section affected only data on larger time scale. For short period of time (a few hours $\sim$ duration of the transit) we did not detected this effect. Therefore, we could derive the radial velocity diagram (RV measurements versus time graph) for each full-night observation.

From 8 full-night observing campaigns only 4 of them were done during the MASCARA-2b transit. For fitting we used the interval of $4900 - 6300$A divided into 10 overlapping intervals of 500 A as before. We chose one of the spectra from the particular night for the template spectrum. As the result we got 4 RV diagrams (one for each transit night — figures 5.3, 5.4, 5.5 and 5.6).

Since the radial velocities are close to zero[1] when the exoplanet is transiting, the average value should approach to zero. Thanks that we could subtract a median value from the RVs. The shape of the RV curve did not change while the whole data set was moved to zero level. We applied this procedure for five nights — the spectra from 2018-08-26 were included as well, since they are close to the transit. They are not taken during the transit, but close to it. Because the time offset is small, we could still include it. After this step, we combined all data into the single radial velocity diagram (Figure 5.7).

5.3 Rossiter-McLaughlin effect

From four transit nights only 2018-10-21 covers the transit in its full length. Thanks to the sufficient number of spectra we can see the whole radial velocity curve (Figure 5.6). An RV variation is seen on the diagram. We consider this anomaly to be caused by the Rossiter-McLaughlin effect. To verify this, we can compare our results with result of Lund et al. (2017) [25], who detected the effect for MASCARA-2 as well. They detected the variations in RVs with an amplitude approximately $2\,\mathrm{km\cdot s^{-1}}$ (Lund et al. 2017 [25], Figure 9).

For illustration we created a simple model of the R-M effect for MASCARA-2 and compared it with the data (see Figure 5.8). We used PHOEBE — Eclipsing Binary Modeling Software. We used the script available at [37] (Prša et al. 2016 [38]). The model is based on parameters from tables 3.1 and 3.2 (values from Lund et al. 2017 [25]). It is not a fit of the data but rather a quick look, as the further analysis is beyond the scope of this thesis.

In our data we can see that the RV amplitude is approximately $2.5\,\mathrm{km\cdot s^{-1}}$ with an average standard deviation approximately $0.33\,\mathrm{km\cdot s^{-1}}$. The amplitude corresponds to the Lund's analysis [25]. Although the RV variation is visible,

[1] When the exoplanet is transiting its parent star, its movement is perpendicular to the observer's line of sight. Therefore it is not changing its relative radial velocity in respect to the observer.

model does not match the data well. Therefore, more thorough analysis of the data is needed. In the next step, we will investigate the stability of the data over one night and we will try to remove the systematic shifts.

5.4 Limits of OES

In order to get more spectra during the transit nights we chose shorter exposure times. That led to the decrease of SNR. However, as the SNR shows to be crucial parameter for precision of the RV determination, for future observation using of the longer exposure times will be optimal. On the other hand, with long exposures it will not be possible to see the RM effect.

The precision we got with SNR ~ 40 is good enough for the safe confirmation of the exoplanet candidates. With higher SNR (good weather conditions, exposure al least 1200 and more) we could reach even higher precision than $0.3\,\mathrm{km\cdot s^{-1}}$. That could lead to more detailed analysis of the stellar spectra. The correct target selection is important as well, since the stellar parameters (e.g. brightness, spectral type etc.) have a significant impact on the spectrum and its processing.

As shown before, when having an optimal data set (e.g. as 2018-10-21) we can see an indication of the Rossiter-McLaughlin effect. Using more precise analysis we should be able to confirm detection of the effect. This supports suitability of the 2-meter Perek telescope for follow-up observation of the exoplanet candidates.

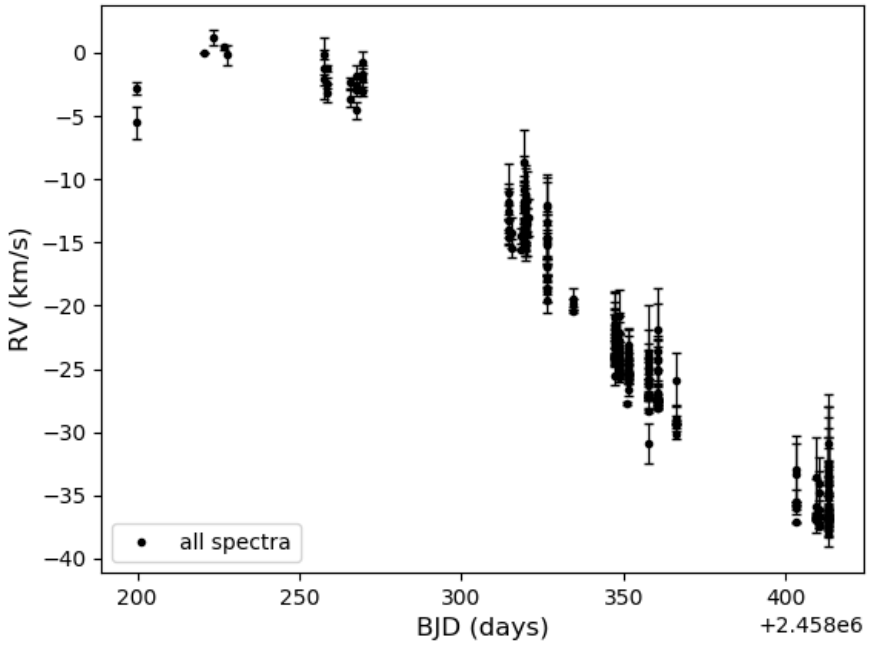

Figure 5.1: Radial velocities affected by the systematic shift in time. All spectra included. Template frame for RVs taken 2018-04-11 (exposure 1800 s, SNR 43).

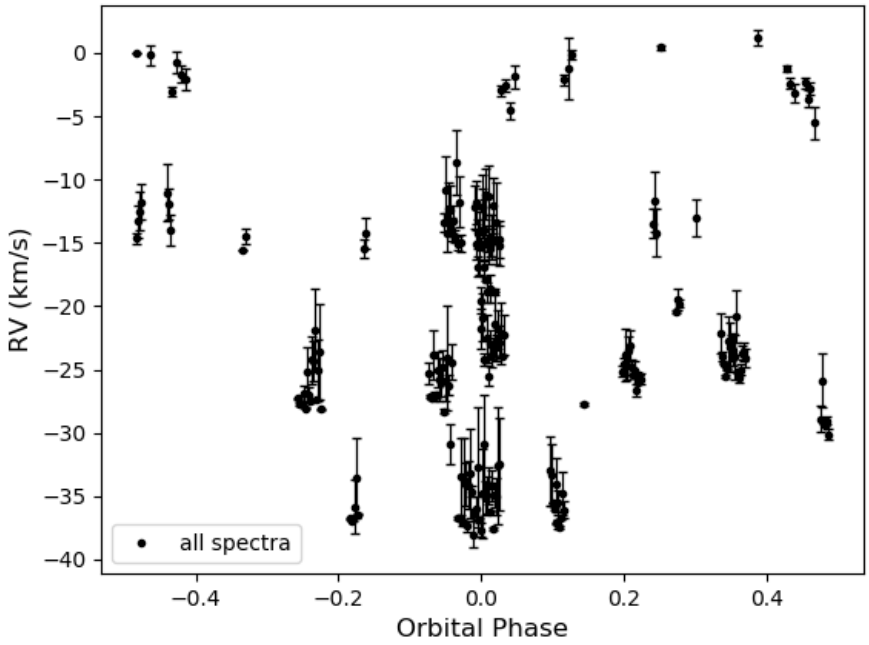

Figure 5.2: Phase diagram affected by the systematic shift. All spectra included. Template frame for RVs taken 2018-04-11 (exposure 1800 s, SNR 43).

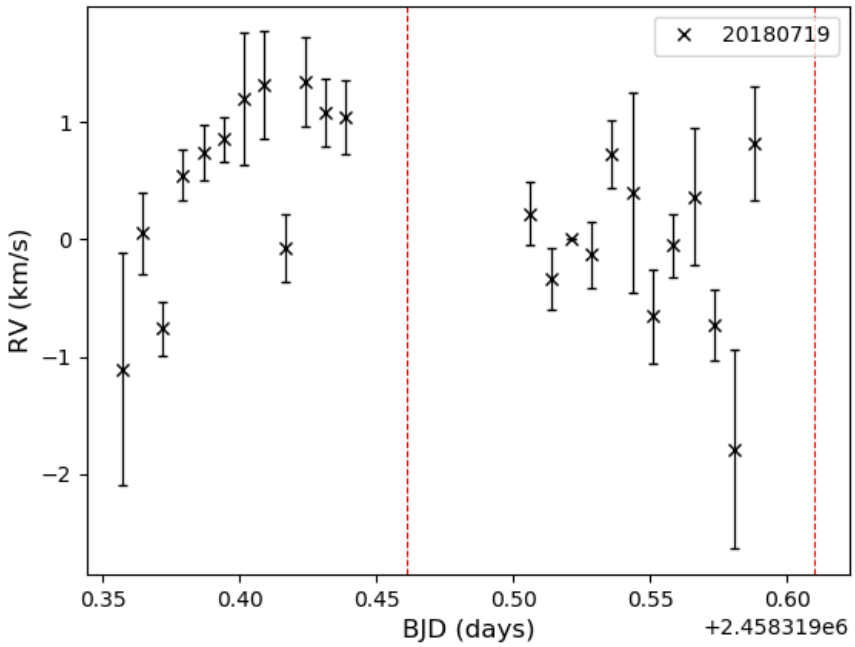

Figure 5.3: RV diagram for 2018-07-19. Red lines show the time of the first and the last contact of transit.

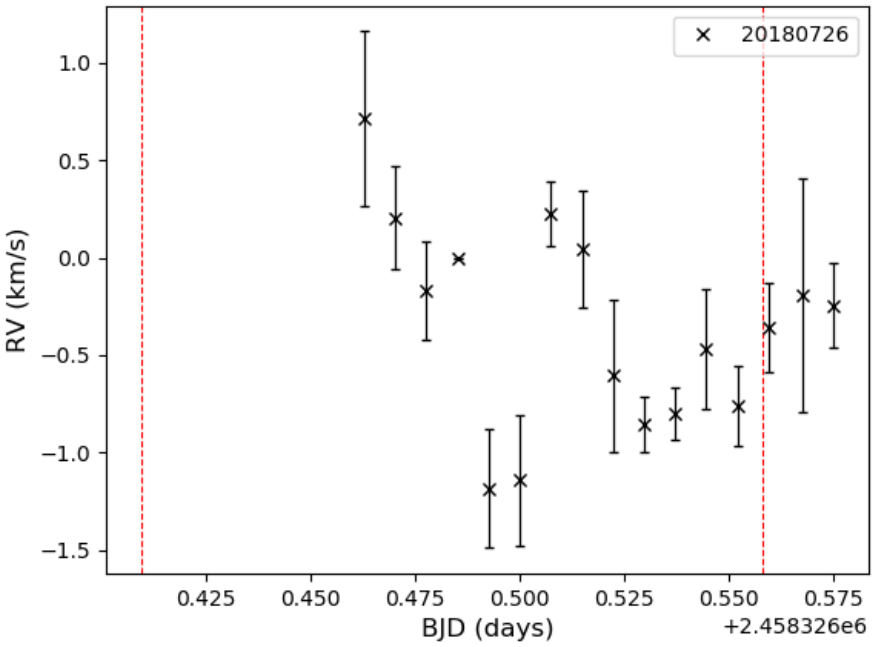

Figure 5.4: RV diagram for 2018-07-26. Red lines show the time of the first and the last contact of transit.

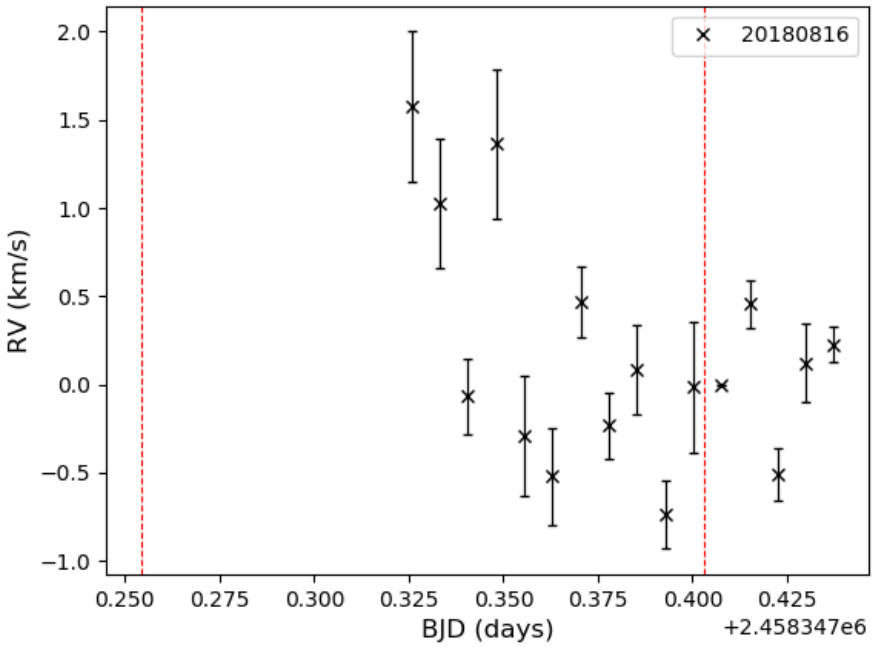

Figure 5.5: RV diagram for 2018-08-16. Red lines show the time of the first and the last contact of transit.

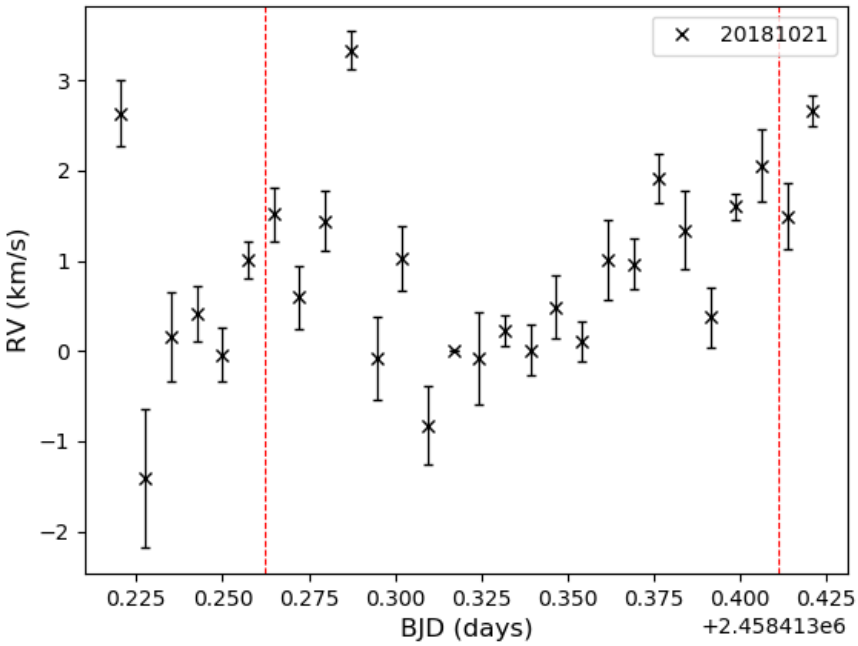

Figure 5.6: RV diagram for 2018-10-21. Red lines show the time of the first and the last contact of transit. We assume the detection of the RM effect in this data.

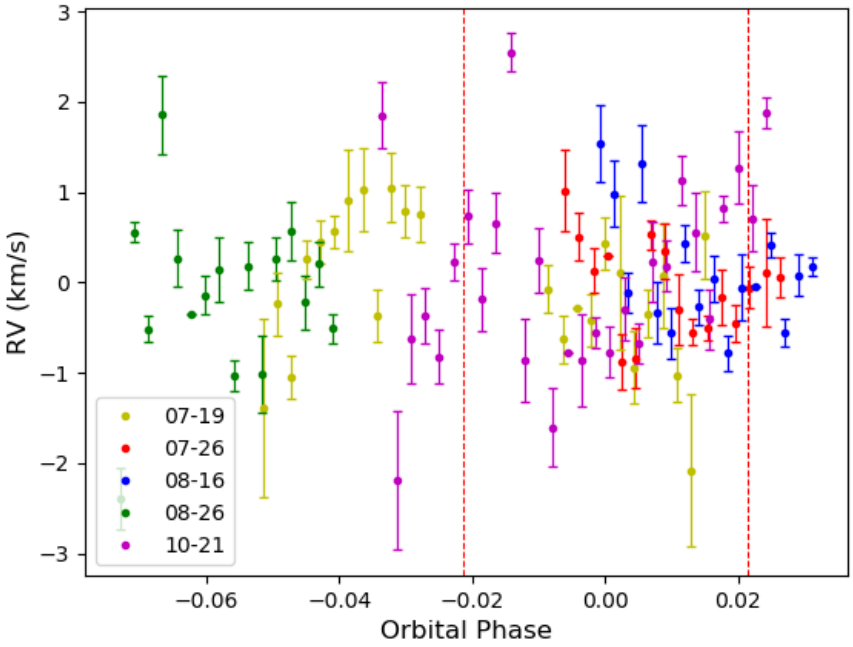

Figure 5.7: Phase diagram of the radial velocities in transit. Data of four transiting nights and one close to transit (2018-08-26) are illustrated. Red lines show the time of the first and the last contact of transit.

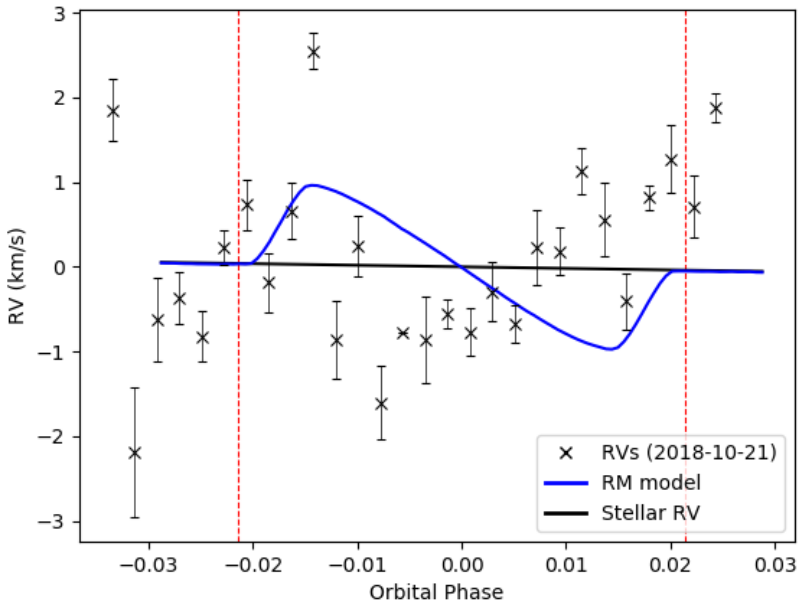

Figure 5.8: An indication of the Rossiter-McLaughlin effect in MASCARA-2 spectrum. The data from night 2018-10-21 are combined with a simple model of the RM effect. Red lines show the time of the first and the last contact of transit.

Summary

In this thesis we presented the results of follow-up observations of the exoplanet MASCARA-2b. All the data were acquired with OES echelle spectrograph installed at Perek Telescope at AI CAS in 2018 (Table 3.3). We optimized the reduction pipeline and the radial velocity determination for MASCARA-2 as an A-type star.

We were not able to create and analyse the long term radial velocity diagram due to the systematic deviation in data. We detected it as the shift in radial velocities which increases in time (Figure 5.1). This will be a subject of further analysis. As the shift did not occur on the short time scale we were able to analyse the full-night transit observations. We showed the radial velocity diagrams of 4 transit nights out of 8 full-night observation campaigns (Figures 5.3, 5.4, 5.5 and 5.6).

With the normalization of the radial velocities from each night to the zero level (done as the subtraction of medial RV value of the particular night) we combined the RVs from transit nights and one close-to-transit night into the transit radial velocity phase diagram (Figure 5.7). As the subject of future work we want to detect the exo-atmospheres (Murgas et al. 2018 [31]). Therefore, a large data set of transit spectra is needed.

We showed an indication of the Rossiter-McLaughlin effect in the data from 2018-10-21. A model combined with the observed data is shown on Figure 5.8. Although the RV variation is visible, we need a more thorough analysis of the data to confirm the effect.

In conclusion, the results presented in this thesis show limits of the 2-meter Perek telescope for the follow-up observations of the exoplanet candidates. We acquired radial velocities with the precision of $\sim 0.3\,\mathrm{km\cdot s^{-1}}$. However, this is not the limit. The accuracy can be increased in case of spectra with SNR higher than 40. An indication of the Rossiter-McLaughlin effect supports suitability of Perek telescope for the follow-up observations.

The presented results will be used in the next follow-up observations. We recommend to choose targets carefully and to optimize the observation strategy. Since high SNR is crucial for the accuracy of RV measurements, we suggest to use an exposure time at least 1800 seconds or even 2×1800 seconds combined to boost the SNR. However, for detection of the Rossiter-McLaughlin effect a compromise between exposure time and SNR has to be found. We recommend to increase the exposure time to 900 or 1200 seconds. A careful reduction of instrumental shifts will be necessary in future work.

References

[1] Addison B.C., Tinney C.G., Wright D.J., Bayliss D. (2018): Spin-orbit Alignment for Three Transiting Hot Jupiters: WASP-103b, WASP-87b, and WASP-66b. *ApJ* **823** 1, 29

[2] Agol E., Fabrycky D.C. (2018): Transit-Timing and Duration Variations for the Discovery and Characterization of Exoplanets; Handbook of Exoplanets, editors H. Deeg H., Belmonte J.A, *Springer International Publishing AG*, part of Springer Nature, id.2, ISBN 978-3-319-55332-0

[3] Baglin A., Auvergne M., Barge P., et al. (2006): Scientific Objectives for a Minisat: CoRoT. *Proceedings of The CoRoT Mission Pre-Launch Status - Stellar Seismology and Planet Finding* (ESA SP-1306). Edited by Fridlund M., Baglin A., Lochard J., Conroy L., ISBN 92-9092-465-9 p.33

[4] Beaulieu J.-P., Bennett D.P., Fouqué P., et al. (2006): Discovery of a cool planet of 5.5 Earth masses through gravitational microlensing. *Nature* **439**, 437–440

[5] Benedict G.F., McArthur B.E., Gatewood G., et al. (2006): The Extrasolar Planet epsilon Eridani b - Orbit and Mass. *AJ* **132** 5, 2206–2218

[6] Borucki W.J. (2016): KEPLER Mission: development and overview *Rep. Prog. Phys.* **79**, 036901

[7] Boué G., Montalto M., Boisse I., et al. (2013): New analytical expressions of the Rossiter-McLaughlin effect adapted to different observation techniques. *A&A* **550**, A53

[8] Bozza V., Mancini L., Sozzetti A. (2016): Methods of Detecting Exoplanets. 1st edition, Switzerland: *Springer International Publishing*, ISBN 978-3-319-27456-0

[9] Campbell B., Walker G.A.H. (1979): Precision radial velocities with an absorption cell. *Astronomical Society of the Pacific, Publications* **91**, 540-545

[10] Charbonneau D., Brown T.M., Latham D.W., Mayor M. (2000): Detection of Planetary Transits Across a Sun-like Star. *ApJ* **529** 1, L45–L48

[11] Charbonneau D., Brown T.M., Noyes R.W., Gilliland R.L. (2002): Detection of an Extrasolar Planet Atmosphere. *ApJ* **568** 1, 377–384

[12] Dvořáková J. (2018): Studium stability Ondřejovského ešeletového spektrografu (OES). Opvava. Bachelor's thesis. Slezská univerzita v Opavě, Filozoficko-přírodovědecká fakulta, Ústav fyziky. Supervised by Klocová T.

[13] Dupkala D. (2018): Characterization of exoplanetary candidates from mission K2 — measurements of radial velocities. Ondřejov. Student Faculty Grant summary, Charles University, Faculty of Mathematics and Physics. Supervised by Kabath P., Skarka M.

[14] Fischer D., Anglada-Escude G., Arriagada P., et al. (2016): State of the Field: Extreme Precision Radial Velocities. *PASP* **128** 964, 066001

[15] Furlan E., Ciardi D.R., Everett M.E., et al. (2017): The Kepler Follow-Up Observation Program. I. A Catalog of Companions to Kepler Stars from High-Resolution Imaging. *AJ* **153** 2, 71

[16] Griffin R. and R. (1973): On the Possibility of Determining Stellar Radial Velocities to 0.01 $\mathrm{km \cdot s^{-1}}$. *MNRAS* **162**, 243–253

[17] Guenther E.W., Wuchterl G. (2003): Companions of old brown dwarfs, and very low mass stars. *A&A* **401**, 677–683

[18] HD 185603. [online] SIMBAD, Centre de données astronomiques de Strasbourg. Retrieved 2019-05-02 from `http://simbad.u-strasbg.fr/simbad/sim-id?protocol=html&Ident=HD%20185603`

[19] Henry G.W., Marcy G., Butler R.P., Vogt S.S. (1999): HD 209458. *IAU Circ.*, No. **7307**, #1. Edited by Green D.W.E.

[20] Jacob A.P., Bedding T.R., Robertson J.G., Scholz M. (2000): Wavelength dependence of angular diameters of M giants: an observational perspective. *MNRAS* **312** 4, 733–746

[21] Kabáth P., Skarka M., Sabotta S., Guenther E. (2019): The role of small telescopes as a ground-based support for exoplanetary space missions. *Contrib. Astron. Obs. Skalnaté Pleso* **49**, 1–8

[22] Kabáth P., Žák J., Boffin H.M.J., et al (2019): Detection limits of exoplanetary atmospheres with 2-m class telescopes. *PASP*, Accepted in May 2019

[23] Koubský P., Mayer P., Čáp J., et al. (2004): Ondřejov Echelle Spectrograph – OES. *Publ. Astron. Ins. ASCR* **92**. 37–43

[24] Kuzuhara M., Tamura M., Kudo T., et al. (2013): Direct imaging of a cold Jovian exoplanet in orbit around the Sun-like star GJ 504. *ApJ* **774**, 11–18

[25] Lund M.B., Rodriguez J.E., Zhou G., et al. (2017): KELT-20b: A giant planet with a period of $P \sim 3.5$ days transiting $V \sim 7.6$ early A star HD 185603. *AJ* **154**, 194

[26] Marcy G.W., Butler R.P., Williams E., et al. (1997): The planet around 51 Pegasi. *ApJ* **481**, 926–935

[27] Martin D.V., Fabrycky D.C., Montet B.T. (2019): Transits of Inclined Exomoons—Hide and Seek and an Application to Kepler-1625. *The ApJ Letters*, **875** 2, L25

[28] Mayor M., Queloz D. (1995): A Jupiter-mass companion to a solar–type star. *Nature* **378**, 355–359

[29] McLaughlin D.B. (1924): Some results of a spectrographic study of the Algol system. *ApJ* **60**, 22–31

[30] Monteiro M.J.P.F.G., Lebreton Y., Montalban J., et al. (2006): Report on the CoRoT Evolution and Seismic Tools Activity. *Proceedings of The CoRoT Mission Pre-Launch Status – Stellar Seismology and Planet Finding* (ESA SP-1306). Edited by Fridlund M., Baglin A., Lochard J., Conroy L., ISBN 92-9092-465-9 p.363

[31] Murgas F., Chen G., Pallé E., et al. (2018): The GTC exoplanet transit spectroscopy survey X. Stellar spots versus Rayleigh scattering: the case of HAT-P-11b. *A&A* **622**, A172

[32] Narita N., Hirano T., Sanchis-Ojeda R., et al. (2010): The Rossiter-McLaughlin Effect of the Transiting Exoplanet XO-4b. *Publications of the Astronomical Society of Japan* **62** 6, L61–L65

[33] Nortmann L., Pallé E., Salz M., et al. (2018): Ground-based detection of an extended helium atmosphere in the Saturn-mass exoplanet WASP-69b. *Science* **362** 6421, 1388-1391

[34] Nutzman P., Charbonneau D., Winn J.N., et al. (2009): A Precise Estimate of the Radius of the Exoplanet HD 149026b from Spitzer Photometry. *ApJ* **692** 1, 229–235

[35] Pepe F., Molaro P., Cristiani S., et al. (2014): ESPRESSO: The next European exoplanet hunter. *AN* **335** 1, 8–20

[36] Perryman M.A. (2000): Extra-solar planets. Rept. Prog. Phys. 63, 1209–1272

[37] PHOEBE 2.0 Documentation: Rossiter-McLaughlin Effect, [online] PHOEBE Development Team (2016). Retrieved 2018-05-10 from `http://www.phoebe-project.org/docs/2.0/examples/rossiter_mclaughlin`

[38] Prša A., Conroy K.E., Horvat M., et al. (2016): Physics Of Eclipsing Binaries. II. Toward the Increased Model Fidelity. *The Astrophysical Journal Supplement Series* **227** 2, 29

[39] Pych, W. (2004): A Fast Algorithm for Cosmic-Ray Removal from Single Images. *PASP* **116**, 148–153

[40] Ricker G.R., Winn J.N., Vanderspek R., et al. (2015): The Transiting Exoplanet Survey Satellite. *J. Astron. Telesc. Instrum. Syst.* **1**(1), 014003

[41] Rossiter R.A. (1924): On the detection of an effect of rotation during eclipse in the velocity of the brigher component of beta Lyrae, and on the constancy of velocity of this system. *ApJ* **60**, 15–21

[42] Sabotta S., Kabáth P., Korth J., et al. (2019): Occurence of close-in, massive planets of A-type stars from Kepler. *Submitted to MNRAS* (May 2019)

[43] Santerne A., Díaz R.F., Almenara J.-M., et al. (2013): Astrophysical false positives in exoplanet transit surveys: why do we need bright stars? *Proceedings of the Annual meeting of the French Society of Astronomy and Astrophysics* (SF2A-2013). Edited by Cambresy L., Martins F., Nuss E., Palacios A., 555-560

[44] Silvotti R., Schuh S., Janulis R., et al. (2007): A giant planet orbiting the extreme horizontal branch star V 391 Pegasi. *Nature* **449**, pages 189–191

[45] Sing D.K., Fortney J.J., Nikolov N., et al. (2016): A continuum from clear to cloudy hot-Jupiter exoplanets without primordial water depletion. *Nature* **529**, 59–62

[46] Šlechta M. (2004): OES - Ondřejovský ešeletový spektrograf, [online] Article for IAN, Retrieved 2019-04-26 from `https://stelweb.asu.cas.cz/~slechta/OES/pro-ian/`

[47] Šlechta M., Škoda P. (2002): 2-meter telescope devices: Coudé slit spectrograph and HEROS. *Publ. Astron. Ins. ASCR* **60**. 1–4

[48] Stellar Physics Department (2018), Ondrejov Perek 2m Telescope, [online] AI CAS. Retrieved 2019-04-24 from `https://stelweb.asu.cas.cz/web/index.php?pg=2m_telescope`

[49] Struve O. (1952): Proposal for a project of high-precision stellar radial velocity work. *The Observatory* **72**, 199-200

[50] Talens G.J.J., Justesen A.B., Albrecht S., et al. (2018): MASCARA-2b A hot Jupiter transiting the $m_V = 7.6$ A-star HD 185603. *A&A* **612**, A57

[51] Triaud A.H.M.J. (2018): The Rossiter-McLaughlin Effect in Exoplanet Research; Handbook of Exoplanets, editors Deeg H., Belmonte J.A, *Springer International Publishing AG*, part of Springer Nature, id.2, ISBN 978-3-319-55332-0

[52] Van Cleve J.E., Caldwell D.A. (2009): Kepler Instrument Handbook. *NASA*, KSCI-19033-001

[53] WASP Planets (2016): Spin-orbit alignments for three more WASP planets. [online] Keele University exoplanet group. Retrieved 2019-04-28 from `https://wasp-planets.net/2016/03/21/spin-orbit-alignments-for-three-more-wasp-planets/`

[54] Winn J.N. (2010): Transits and Occultations; Exoplanets, editor Seager S., Tucson, AZ: *University of Arizona Press*, ISBN 978-0-8165-2945-2

[55] Wolszczan A. (1994): Confirmation of Earth-Mass Planets Orbiting the Millisecond Pulsar PSR 1257+12. *Science* **264**, 538–542

[56] Wolszczan A., Frail D.A. (1992): A Planetary System Around Millisecond Pulsar PSR 1257+12. *Nature* **355**, 145–147

List of Figures

1.1 Illustration of the Rossiter-McLaughlin effect for three exoplanets: WASP-66b, WASP-87b and WASP-103b. The color on the star disk corresponds to the radial velocities of the various parts of the surface. Image taken from [53] based on the results of Addison et al. 2018 [1]. 9

2.1 Perek 2-meter telescope at Ondřejov observatory. Picture taken from the web pages of the Stellar dept. of AI CAS [48]. 10
2.2 Scheme of the OES spectrograph. **A** The slit, **B** first collimator, **C** echelle grating, **D** parabolic mirror, **E** small flat mirror, **F** secondary colimator, **G** crossdisperser, **H** camera with the CCD chip (Šlechta [46]). 12

3.1 MASCARA-2, raw image (taken 2018-04-11, exposure time 1800 s). 17
3.2 MASCARA-2, image with cosmic rays removed, bias, flat and bad pixels correction (taken 2018-04-11, exposure time 1800 s). 17
3.3 Bias correction frame (raw image, taken 2018-04-11, exposure time 0 seconds). 18
3.4 Th-Ar comparison frame (raw image, taken 2018-04-11, exposure time 140 seconds). 18
3.5 Flat lamp correction frame (raw image, taken 2018-04-11, exposure time 40 seconds). 18
3.6 Vega (alp Lyr), aperture template frame (raw image, taken 2018-04-11, exposure time 120 seconds). 18

4.1 Aperture definition using the *apall* task. Vega is used as the template spectrum, exposure 30 seconds, 2018-08-20. 21
4.2 Spectral line identification using the *ecidentify* task. Identification is done on ThAr comparison spectrum from 2018-08-20. 21
4.3 Reduced spectrum of Vega from 2018-04-11, exposure 120 s. . . . 23
4.4 Reduced spectrum of MASCARA-2 from 2018-04-11, exposure 1800 s. 24
4.5 Reduced spectrum of MASCARA-2 from 2018-10-21, exposure 600 s. 24

5.1 Radial velocities affected by the systematic shift in time. All spectra included. Template frame for RVs taken 2018-04-11 (exposure 1800 s, SNR 43). 28
5.2 Phase diagram affected by the systematic shift. All spectra included. Template frame for RVs taken 2018-04-11 (exposure 1800 s, SNR 43). 28
5.3 RV diagram for 2018-07-19. Red lines show the time of the first and the last contact of transit. 29
5.4 RV diagram for 2018-07-26. Red lines show the time of the first and the last contact of transit. 29
5.5 RV diagram for 2018-08-16. Red lines show the time of the first and the last contact of transit. 30

5.6 RV diagram for 2018-10-21. Red lines show the time of the first and the last contact of transit. We assume the detection of the RM effect in this data. 30
5.7 Phase diagram of the radial velocities in transit. Data of four transiting nights and one close to transit (2018-08-26) are illustrated. Red lines show the time of the first and the last contact of transit. 31
5.8 An indication of the Rossiter-McLaughlin effect in MASCARA-2 spectrum. The data from night 2018-10-21 are combined with a simple model of the RM effect. Red lines show the time of the first and the last contact of transit. 31

List of Tables

3.1 Basic parameters of HD 185603. References: [1]SIMBAD Database [18], [2]Lund et al. 2017 [25], [3]Talens et al. 2018 [50] 13
3.2 Planet parameters of MASCARA-2b. Compared values taken from two different papers (Lund et at. 2017 [25] & Talens et al. 2018 [50]). [a]3σ mass limit. 13
3.3 MASCARA-2b data set. Table shows date and number of spectra obtained during the observation. 15

4.1 Template frames used for aperture definition. Vega (alp Lyr) was used as a reference star. Template numbers correspond to the templates in Table 3.3. RMS value shows an accuracy of the wavelength solution for ThAr spectral lines identification. 20

A.1 Radial velocity measurements from 2018-07-19 (transit campaign). 41
A.2 Radial velocity measurements from 2018-07-26 (transit campaign). 41
A.3 Radial velocity measurements from 2018-08-16 (transit campaign). 42
A.4 Radial velocity measurements from 2018-08-17. 42
A.5 Radial velocity measurements from 2018-08-20. 42
A.6 Radial velocity measurements from 2018-08-26. (transit campaign) 43
A.7 Radial velocity measurements from 2018-08-29. 43
A.8 Radial velocity measurements from 2018-10-21. (transit campaign) 43
A.9 Radial velocity measurements performed on the full data set. . . . 44
A.10 Radial velocity measurements performed on the full data set. . . . 45

List of Abbreviations

AI CAS	Astronomical Institute of the Czech Academy of Sciences
AJ	The Astronomical Journal
AN	Astronomische Nachrichten (Astronomical Notes)
ApJ	The Astrophysical Journal
A&A	Astronomy & Astrophysics
AO	Adaptive Optics
BJD	Barycentric Julian Date
CCD	Charge-Coupled Device
CoRoT	Convection, Rotation and planetary Transits
DCR	Detect and Remove Cosmic Rays
FOV	Field Of View
HJD	Heliocentric Julian Date
IRAF	Image Reduction and Analysis Facility
JD	Julian Date
KELT	Kilodegree Extremely Little Telescope
KELT-FUN	KELT Follow-Up Network
MNRAS	Monthly Notices of the Royal Astronomical Society
NOAO	National Optical Astronomy Observatory
OES	Ondřejov Echelle Spectrograph
PASP	Publications of the Astronomical Society of the Pacific
PHOEBE	PHysics Of Eclipsing BinariEs
RM	Rossiter-McLaughlin effect
RV	Radial Velocity
SNR	signal to noise ratio
TESS	Transiting Exoplanet Survey Satellite
ThAr	Thorium-Argon (lamp)

A. Attachments

A.1 Results of RV measurements

Here we present the results of radial velocity measurements for the full-night campaigns (Figures A.1 to A.8) and for the full data set as well (Figures A.9 and A.10). The RV template frames are highlighted and both RV and its error s_{rv} are zero. For the full data set analysis a spectrum from night 2018-04-11 was used as the RV template. The errors are calculated as described before (see Formula (5.1)).

BJD (days)	RV ($\mathrm{km \cdot s^{-1}}$)	s_{rv} ($\mathrm{km \cdot s^{-1}}$)	BJD (days)	RV ($\mathrm{km \cdot s^{-1}}$)	s_{rv} ($\mathrm{km \cdot s^{-1}}$)
2458319.356971	-1.1048	0.9863	2458319.506241	0.2164	0.2672
2458319.364411	0.0516	0.3446	2458319.513681	-0.3385	0.2591
2458319.371851	-0.7613	0.2335	**2458319.521131**	**0.0000**	**0.0000**
2458319.379301	0.5482	0.2155	2458319.528571	-0.1296	0.2823
2458319.386741	0.7401	0.2352	2458319.536011	0.7260	0.2928
2458319.394181	0.8517	0.1857	2458319.543451	0.3944	0.8543
2458319.401621	1.2020	0.5654	2458319.550891	-0.6541	0.3994
2458319.409061	1.3165	0.4543	2458319.558341	-0.0530	0.2659
2458319.416511	-0.0783	0.2869	2458319.565781	0.3647	0.5830
2458319.423951	1.3394	0.3821	2458319.573221	-0.7350	0.3033
2458319.431391	1.0807	0.2849	2458319.580661	-1.7893	0.8490
2458319.438831	1.0447	0.3128	2458319.588111	0.8157	0.4853

Table A.1: Radial velocity measurements from 2018-07-19 (transit campaign).

BJD (days)	RV ($\mathrm{km \cdot s^{-1}}$)	s_{rv} ($\mathrm{km \cdot s^{-1}}$)	BJD (days)	RV ($\mathrm{km \cdot s^{-1}}$)	s_{rv} ($\mathrm{km \cdot s^{-1}}$)
2458326.462951	0.7141	0.4475	2458326.522491	-0.6049	0.3915
2458326.470401	0.2043	0.2658	2458326.529931	-0.8542	0.1437
2458326.477841	-0.1693	0.2534	2458326.537371	-0.7994	0.1346
2458326.485281	**0.0000**	**0.0000**	2458326.544821	-0.4707	0.3071
2458326.492721	-1.1861	0.3046	2458326.552261	-0.7608	0.2054
2458326.500161	-1.1425	0.3339	2458326.559701	-0.3564	0.2301
2458326.507611	0.2257	0.1661	2458326.567881	-0.1897	0.6006
2458326.515051	0.0453	0.3005	2458326.575331	-0.2475	0.2174

Table A.2: Radial velocity measurements from 2018-07-26 (transit campaign).

BJD (days)	RV ($km \cdot s^{-1}$)	s_{rv} ($km \cdot s^{-1}$)	BJD (days)	RV ($km \cdot s^{-1}$)	s_{rv} ($km \cdot s^{-1}$)
2458347.325770	1.5758	0.4239	2458347.385300	0.0843	0.2536
2458347.333210	1.0243	0.3660	2458347.392740	-0.7355	0.1954
2458347.340650	-0.0670	0.2167	2458347.400190	-0.0137	0.3688
2458347.348090	1.3624	0.4222	**2458347.407630**	**0.0000**	**0.0000**
2458347.355530	-0.2879	0.3396	2458347.415070	0.4559	0.1380
2458347.362980	-0.5216	0.2761	2458347.422510	-0.5108	0.1488
2458347.370420	0.4679	0.2032	2458347.429950	0.1229	0.2257
2458347.377860	-0.2320	0.1876	2458347.437400	0.2275	0.1020

Table A.3: Radial velocity measurements from 2018-08-16 (transit campaign).

BJD (days)	RV ($km \cdot s^{-1}$)	s_{rv} ($km \cdot s^{-1}$)	BJD (days)	RV ($km \cdot s^{-1}$)	s_{rv} ($km \cdot s^{-1}$)
2458348.491200	**0.0000**	**0.0000**	2458348.558180	0.3261	0.3381
2458348.498650	0.2917	0.1890	2458348.565620	0.6095	0.3831
2458348.506090	-0.6447	0.6039	2458348.573070	0.5247	0.4181
2458348.513530	0.1050	0.4150	2458348.580510	-0.7568	0.5510
2458348.520970	-0.1962	0.5859	2458348.587950	0.1512	0.3280
2458348.528410	-0.9003	0.6319	2458348.595390	0.7873	0.3914
2458348.535860	-0.1812	0.3213	2458348.602830	-1.1140	0.7790
2458348.543300	0.1306	0.3055	2458348.610280	1.1820	0.4982
2458348.550740	0.9631	0.2165			

Table A.4: Radial velocity measurements from 2018-08-17.

BJD (days)	RV ($km \cdot s^{-1}$)	s_{rv} ($km \cdot s^{-1}$)	BJD (days)	RV ($km \cdot s^{-1}$)	s_{rv} ($km \cdot s^{-1}$)
2458351.491580	0.4674	0.2883	2458351.543670	-0.4396	0.4730
2458351.499020	1.3439	0.6269	2458351.551110	-0.0912	0.4060
2458351.506460	-0.0147	0.2434	2458351.558550	-1.2735	0.5534
2458351.513900	**0.0000**	**0.0000**	2458351.566000	0.6839	0.3027
2458351.521340	0.6601	0.2283	2458351.573440	0.0469	0.2074
2458351.528790	-0.0220	0.2225	2458351.580880	0.2907	0.4985
2458351.536230	-0.1067	0.4224			

Table A.5: Radial velocity measurements from 2018-08-20.

BJD (days)	RV ($km \cdot s^{-1}$)	s_{rv} ($km \cdot s^{-1}$)	BJD (days)	RV ($km \cdot s^{-1}$)	s_{rv} ($km \cdot s^{-1}$)
2458357.497180	-2.0525	0.3334	2458357.556720	-0.6914	0.1736
2458357.504620	0.9024	0.1166	2458357.564160	0.5276	0.2585
2458357.512060	-0.1714	0.1496	2458357.571600	-0.6699	0.4300
2458357.519510	2.2023	0.4379	2458357.579040	0.6004	0.2412
2458357.526950	0.6107	0.3152	2458357.586480	0.9105	0.3226
2458357.534390	**0.0000**	**0.0000**	2458357.593930	0.1207	0.2912
2458357.541830	0.2002	0.2096	2458357.601370	0.5507	0.2491
2458357.549270	0.4852	0.3633	2458357.608810	-0.1670	0.1608

Table A.6: Radial velocity measurements from 2018-08-26. (transit campaign)

BJD (days)	RV ($km \cdot s^{-1}$)	s_{rv} ($km \cdot s^{-1}$)	BJD (days)	RV ($km \cdot s^{-1}$)	s_{rv} ($km \cdot s^{-1}$)
2458360.331410	-0.0560	0.2821	2458360.398390	-1.1389	0.3809
2458360.338850	**0.0000**	**0.0000**	2458360.405830	-0.7614	0.2652
2458360.346290	0.0003	0.1998	2458360.413270	-1.2714	0.3323
2458360.353740	-0.7399	0.3093	2458360.420710	-0.1520	0.1974
2458360.361180	-2.4774	0.8767	2458360.428150	-0.1695	0.3390
2458360.368620	-0.2396	0.5897	2458360.435600	-0.4884	0.3465
2458360.376060	-0.0031	0.3324	2458360.443040	-1.5498	0.3549
2458360.383500	-0.5608	0.0906			

Table A.7: Radial velocity measurements from 2018-08-29.

BJD (days)	RV ($km \cdot s^{-1}$)	s_{rv} ($km \cdot s^{-1}$)	BJD (days)	RV ($km \cdot s^{-1}$)	s_{rv} ($km \cdot s^{-1}$)
2458413.220189	2.6333	0.3647	2458413.324379	-0.0848	0.5115
2458413.227629	-1.4085	0.7737	2458413.331819	0.2264	0.1780
2458413.235079	0.1550	0.4971	2458413.339259	0.0130	0.2792
2458413.242519	0.4151	0.2998	2458413.346699	0.4874	0.3454
2458413.249959	-0.0387	0.3022	2458413.354139	0.1019	0.2234
2458413.257399	1.0180	0.2043	2458413.361579	1.0024	0.4419
2458413.264839	1.5160	0.2944	2458413.369029	0.9639	0.2786
2458413.272279	0.5990	0.3485	2458413.376469	1.9150	0.2785
2458413.279729	1.4402	0.3284	2458413.383909	1.3404	0.4345
2458413.287169	3.3297	0.2111	2458413.391349	0.3751	0.3362
2458413.294609	-0.0771	0.4629	2458413.398789	1.5979	0.1418
2458413.302049	1.0250	0.3630	2458413.406229	2.0531	0.4025
2458413.309489	-0.8219	0.4399	2458413.413679	1.4925	0.3685
2458413.316929	**0.0000**	**0.0000**	2458413.421119	2.6623	0.1644

Table A.8: Radial velocity measurements from 2018-10-21. (transit campaign)

BJD (days)	RV ($km \cdot s^{-1}$)	s_{rv} ($km \cdot s^{-1}$)	BJD (days)	RV ($km \cdot s^{-1}$)	s_{rv} ($km \cdot s^{-1}$)
2458199.539504	-2.7819	0.5262	2458319.565781	-15.0476	0.6878
2458199.560844	-5.5175	1.2818	2458319.573221	-11.2583	2.3292
2458220.578953	**0.0000**	**0.0000**	2458319.580661	-15.4884	0.5289
2458223.604153	1.1550	0.6132	2458319.588111	-14.9727	1.0888
2458226.609293	0.4241	0.2141	2458320.371481	-13.4778	1.1346
2458227.601503	-0.1748	0.7952	2458320.378921	-11.7117	2.4037
2458257.403572	-2.0981	0.4186	2458320.386361	-14.2024	1.9085
2458257.424902	-1.2132	2.4742	2458320.581941	-12.9702	1.4627
2458257.437392	-0.1089	0.3399	2458326.462951	-15.0975	1.1405
2458258.485322	-1.2617	0.2219	2458326.470401	-16.8593	0.8314
2458258.506652	-2.4129	0.4211	2458326.477841	-15.0002	2.4641
2458258.527982	-3.1899	0.7491	2458326.485281	-19.5292	1.0476
2458265.526872	-2.3499	0.4120	2458326.492721	-12.1021	2.4322
2458265.541262	-3.6255	0.6441	2458326.500161	-16.9359	0.6751
2458267.521292	-2.9390	0.4315	2458326.507611	-17.8175	0.1434
2458267.542622	-2.5518	0.5278	2458326.515051	-18.8993	0.7578
2458267.563952	-4.5456	0.6630	2458326.522491	-14.7126	1.9575
2458267.585292	-1.8761	0.9068	2458326.529931	-18.6516	1.0940
2458269.393872	-3.0648	0.3369	2458326.537371	-14.5470	1.7862
2458269.415212	-0.7379	0.8136	2458326.544821	-12.0331	2.1985
2458269.436542	-1.6573	0.6895	2458326.552261	-18.8505	0.2010
2458269.457872	-2.0525	0.8357	2458326.559701	-13.3955	3.2074
2458314.381671	-14.6329	0.4347	2458326.567881	-15.1805	1.6079
2458314.389111	-13.3116	1.2806	2458326.575331	-14.7175	1.4711
2458314.396561	-12.4832	1.5324	2458334.382771	-20.4346	0.0873
2458314.404001	-11.7441	1.3874	2458334.390211	-19.4983	0.8520
2458314.532281	-11.0287	2.2179	2458334.397651	-19.7652	0.2892
2458314.539721	-11.8983	1.2375	2458347.325770	-21.7747	1.5533
2458314.547161	-13.9662	1.1940	2458347.333210	-20.8558	1.8653
2458315.488731	-15.4621	0.7537	2458347.340650	-24.1485	0.4916
2458315.496181	-14.2437	1.2356	2458347.348090	-24.1716	0.0379
2458318.376081	-15.5519	0.0159	2458347.355530	-22.5460	1.8891
2458318.390471	-14.4425	0.6150	2458347.362980	-25.4916	0.7802
2458319.356971	-13.3585	0.7200	2458347.370420	-22.9732	1.0876
2458319.364411	-10.8585	2.6528	2458347.377860	-23.7955	1.0601
2458319.371851	-14.2128	1.5340	2458347.385300	-23.3806	0.8664
2458319.379301	-12.2677	2.0770	2458347.392740	-21.3938	2.5559
2458319.386741	-12.4137	2.0035	2458347.400190	-23.2857	1.0706
2458319.394181	-13.9304	0.9243	2458347.407630	-21.8028	1.5326
2458319.401621	-13.2332	1.2064	2458347.415070	-22.8028	1.3072
2458319.409061	-14.5268	0.4892	2458347.422510	-22.1200	2.4531
2458319.416511	-8.5974	2.5517	2458347.429950	-23.9081	0.0931
2458319.423951	-15.0461	0.5196	2458347.437400	-22.2194	1.5767
2458319.431391	-11.7523	2.0063	2458348.491200	-22.1042	1.5556
2458319.438831	-14.9981	0.6829	2458348.498650	-23.9238	0.3696
2458319.506241	-12.2037	1.6856	2458348.506090	-24.5079	0.0761
2458319.513681	-11.8115	1.7263	2458348.513530	-25.5143	0.1400
2458319.521131	-14.2779	1.1474	2458348.520970	-24.9516	0.0615
2458319.528571	-15.2278	0.0201	2458348.528410	-22.6919	1.9364
2458319.536011	-15.2364	0.3189	2458348.535860	-23.2161	1.9724
2458319.543451	-12.1921	1.5456	2458348.543300	-23.2733	0.9850
2458319.550891	-13.9571	2.4523	2458348.550740	-23.4111	1.2744
2458319.558341	-11.1522	1.9692	2458348.558180	-23.9720	1.7546

Table A.9: Radial velocity measurements performed on the full data set.

BJD (days)	RV ($km \cdot s^{-1}$)	s_{rv} ($km \cdot s^{-1}$)	BJD (days)	RV ($km \cdot s^{-1}$)	s_{rv} ($km \cdot s^{-1}$)
2458348.565620	-20.8135	2.0507	2458366.354350	-28.8872	0.9919
2458348.573070	-25.1489	0.1146	2458366.361790	-25.8483	2.1076
2458348.580510	-25.6765	0.2936	2458366.369230	-29.2024	0.1201
2458348.587950	-25.0138	0.3924	2458366.376670	-29.3682	0.0682
2458348.595390	-23.6707	0.5816	2458366.384120	-29.0205	0.3219
2458348.602830	-23.5852	0.7302	2458366.391560	-30.1174	0.3998
2458348.610280	-24.1083	0.7081	2458403.246719	-33.0078	2.7804
2458351.303140	-27.7287	0.1526	2458403.254159	-33.2977	2.4068
2458351.491580	-25.1352	0.4314	2458403.261609	-35.5078	0.0352
2458351.499020	-24.6172	0.5847	2458403.269049	-36.0017	0.1118
2458351.506460	-23.8083	2.0854	2458403.276489	-37.1367	0.0772
2458351.513900	-24.7370	0.9956	2458403.283929	-35.5470	0.9881
2458351.521340	-23.4722	1.1248	2458409.227079	-36.7726	0.0528
2458351.528790	-23.0793	1.2165	2458409.234519	-36.9059	0.0566
2458351.536230	-24.8278	0.6344	2458409.241959	-36.7406	0.1682
2458351.543670	-25.4109	0.0706	2458409.249409	-35.8363	2.1518
2458351.551110	-25.0088	0.6412	2458409.256849	-33.5783	3.1319
2458351.558550	-26.6366	0.4643	2458409.264289	-36.4308	0.0382
2458351.566000	-25.9784	0.2167	2458410.225989	-34.0973	2.0993
2458351.573440	-25.4194	0.0191	2458410.233429	-37.2447	0.3481
2458351.580880	-25.7286	0.4489	2458410.240869	-37.4073	0.1271
2458357.497180	-25.2910	0.8408	2458410.248309	-36.7759	0.0238
2458357.504620	-27.1008	0.1261	2458410.255759	-34.7572	1.6982
2458357.512060	-27.2848	0.0179	2458410.263199	-36.0713	0.6518
2458357.519510	-23.7919	1.9309	2458413.220189	-36.6946	0.0868
2458357.526950	-27.0954	0.3373	2458413.227629	-36.7078	0.1116
2458357.534390	-27.0214	0.1989	2458413.235079	-33.3840	3.0315
2458357.541830	-25.0037	1.3585	2458413.242519	-37.0813	0.2724
2458357.549270	-25.7547	1.7381	2458413.249959	-33.7204	3.2657
2458357.556720	-26.0060	1.0679	2458413.257399	-34.0652	1.7104
2458357.564160	-24.7987	1.3322	2458413.264839	-37.3618	0.4242
2458357.571600	-28.3066	0.1613	2458413.272279	-34.1245	1.8497
2458357.579040	-25.8388	1.6045	2458413.279729	-33.2145	3.5153
2458357.586480	-24.0543	4.1152	2458413.287169	-34.6253	0.4282
2458357.593930	-26.2103	0.7685	2458413.294609	-37.9961	1.0806
2458357.601370	-30.8521	1.5934	2458413.302049	-36.3589	0.2084
2458357.608810	-24.4239	1.3902	2458413.309489	-35.9810	0.9089
2458360.331410	-27.2461	0.0680	2458413.316929	-32.7580	4.7491
2458360.338850	-27.6657	0.1189	2458413.324379	-36.8506	0.1894
2458360.346290	-27.6710	0.1233	2458413.331819	-37.6551	0.5577
2458360.353740	-27.6776	0.2245	2458413.339259	-34.7954	3.5025
2458360.361180	-26.8245	0.6073	2458413.346699	-30.8728	3.8749
2458360.368620	-28.0684	0.0680	2458413.354139	-35.1177	1.3012
2458360.376060	-25.1406	1.8563	2458413.361579	-34.9089	1.4191
2458360.383500	-26.9845	0.6494	2458413.369029	-34.2065	1.4603
2458360.390950	-27.4910	0.0584	2458413.376469	-36.2167	0.0459
2458360.398390	-24.2453	1.8854	2458413.383909	-34.1992	1.1891
2458360.405830	-24.3235	1.5629	2458413.391349	-37.5867	0.0789
2458360.413270	-21.8635	3.2256	2458413.398789	-34.8627	0.9968
2458360.420710	-27.4153	0.1116	2458413.406229	-34.9961	1.4750
2458360.428150	-25.0815	2.4293	2458413.413679	-32.6210	4.5974
2458360.435600	-23.6309	3.7729	2458413.421119	-32.5118	3.6428
2458360.443040	-28.1452	0.0419			

Table A.10: Radial velocity measurements performed on the full data set.